JGR Atmospheres

RESEARCH ARTICLE

10.1029/2024JD041090

Dependencies of Simulated Convective Cell and System Growth Biases on Atmospheric Instability and Model Resolution

Zhixiao Zhang[1,2], Adam C. Varble[1,3], Zhe Feng[3], James N. Marquis[3], Joseph C. Hardin[3], and Edward J. Zipser[1]

[1]Department of Atmospheric Sciences, University of Utah, Salt Lake City, UT, USA, [2]Now at Department of Physics, University of Oxford, Oxford, UK, [3]Atmospheric, Climate, and Earth Sciences Division, Pacific Northwest National Laboratory, Richland, WA, USA

Key Points:

- A convection-permitting simulation overestimates the convective contribution to total rainfall, while underestimating stratiform rainfall
- A large excess of simulated shallow convective cells increases as instability decreases, contributing to the stratiform rainfall bias
- Increasing model resolution does not improve convective cell and convective-stratiform rainfall partitioning biases

Supporting Information:

Supporting Information may be found in the online version of this article.

Correspondence to:

A. C. Varble,
adam.varble@pnnl.gov

Citation:

Zhang, Z., Varble, A. C., Feng, Z., Marquis, J. N., Hardin, J. C., & Zipser, E. J. (2024). Dependencies of simulated convective cell and system growth biases on atmospheric instability and model resolution. *Journal of Geophysical Research: Atmospheres*, *129*, e2024JD041090. https://doi.org/10.1029/2024JD041090

Received 1 MAR 2024
Accepted 3 NOV 2024

Author Contributions:

Conceptualization: Zhixiao Zhang, Adam C. Varble
Data curation: Zhixiao Zhang, Adam C. Varble, Zhe Feng, James N. Marquis, Joseph C. Hardin
Formal analysis: Zhixiao Zhang
Funding acquisition: Adam C. Varble, Edward J. Zipser
Investigation: Zhixiao Zhang, Adam C. Varble, Zhe Feng, James N. Marquis
Methodology: Zhixiao Zhang, Adam C. Varble

Abstract This study evaluates convective cell properties and their relationships with convective and stratiform rainfall within a season-long convection-permitting weather research and forecasting simulation over central Argentina using radar, satellite, and radiosonde measurements from the RELAMPAGO-CACTI field campaign. The simulation slightly underestimates radar-estimated rainfall over the ~3.5-month evaluation period but underestimates stratiform rainfall by 46% and overestimates convective rainfall by 43%. As convective available potential energy (CAPE) increases, the convective rainfall overestimation decreases, but the stratiform rainfall underestimation increases such that the contribution of convective to total rainfall remains constantly high biased by ~26%. Overestimated convective rainfall arises from the simulation generating 2.6 times more precipitating convective cells (14,299) than observed by radar (5,662) despite similar observed and simulated cell growth processes, with relatively wide cells contributing mostly to excessive convective rainfall. Relatively shallow cells, typically reaching heights of 4–7 km, contribute most to the cell number bias. This cell number bias increases as CAPE decreases, potentially because cells and their updrafts become narrower and more under-resolved as CAPE decreases. The gross overproduction of precipitating shallow cells leads to overly efficient precipitation and inadequate detrainment of ice aloft, thereby diminishing the formation of robust stratiform rainfall regions. Decreasing model horizontal grid spacing from 3 to 1 or 0.333 km for low (<300 J kg^{-1}) and high CAPE (>1,000 J kg^{-1}) cases results in minimal change to cell number, depth, and convective-to-stratiform partitioning biases. This suggests that improving prediction of these convective properties depends on factors beyond solely increasing model resolution.

Plain Language Summary The ability of a storm-resolving weather model to predict rainfall over central Argentina was evaluated with data from a field campaign. Although the model accurately predicted the total amount of rain, it produced far too much relatively heavy rainfall and not enough light rainfall. The overestimation of heavy rainfall increased as the atmosphere became less favorable for intense storms, which correlated with far too many predicted storm cells, especially ones that were relatively shallow. The excessive frequency of storm cells prevented the formation of widespread lighter rainfall that was much more frequent in observations. Increasing the spatial resolution of the model to better resolve storm circulations did not improve predictions, suggesting model representation of storm precipitation formation, and growth processes requires improvement beyond model resolution to better predict storm rainfall intensities.

1. Introduction

Organized convective clouds critically impact weather (e.g., extreme precipitation and severe winds) and climate (e.g., synoptic waves, intra-seasonal to seasonal oscillations, and decadal teleconnections) through redistributing atmospheric heat, moisture, and momentum (Houze, 2004). Convective regions correspond to net latent heating at nearly all heights, while stratiform regions correspond to net heating in the upper troposphere and net cooling in the lower troposphere (e.g., Liu et al., 2015; Schumacher et al., 2004) with a dependence on the height of condensate transport from convective regions (Han et al., 2019). Relatively greater stratiform contributions to total latent heating integrated in time and space elevate tropical large-scale circulation responses and alter wave propagation from the tropics to extratropics (e.g., Schumacher et al., 2004). Accurate representation of convective-stratiform partitioning by area and precipitation as a function of system life cycle and ambient environmental conditions is crucial for weather and climate prediction.

Project administration: Adam C. Varble, Edward J. Zipser
Resources: Adam C. Varble
Software: Zhixiao Zhang, Zhe Feng, James N. Marquis, Joseph C. Hardin
Supervision: Adam C. Varble
Visualization: Zhixiao Zhang, Zhe Feng
Writing – original draft: Zhixiao Zhang
Writing – review & editing: Zhixiao Zhang, Adam C. Varble, Zhe Feng, James N. Marquis

Weather and climate models have difficulties reproducing observed convective-stratiform partitioning. General circulation models (GCMs) used for long-range climate prediction and global weather models are too coarse to resolve convective-scale processes such that convection parameterizations are needed. However, most sub-grid scale convection parameterizations do not attempt to represent stratiform regions or mesoscale organization. Stratiform precipitation is left to grid scale processes (e.g., Pan & Randall, 1998) or parameterized by semi-empirical relations that link stratiform rainfall to moisture detrainment from the estimated convective vertical mass flux (e.g., Donner, 1993; Donner et al., 2001; Yang et al., 2013). Higher resolution convection-permitting models (CPMs) with usually 4 km or less horizontal grid spacing explicitly allow convection, can resolve mesoscale circulations, and are often able to reproduce observed rainfall totals (e.g., Prein et al., 2013). Nevertheless, CPMs often fail to reproduce observed convective-stratiform area and rainfall partitioning, underestimating the areal coverage and volume of stratiform precipitation while overestimating the areal coverage and volume of convective rainfall (e.g., Caine et al., 2013; Fan et al., 2017; Feng, Leung, et al., 2023; Feng et al., 2018; Hagos et al., 2014; Varble et al., 2011, 2014a, 2014b; Zhang et al., 2021).

Convective cell biases in the model could contribute to errors in simulating convective-stratiform partitioning. Atmospheric circulation boundaries (e.g., fronts, dry lines, terrain flows, boundary layer rolls, and cold pool outflows) spatially aggregate convective cells with modulation by vertical wind shear (e.g., Mulholland et al., 2018; Rotunno et al., 1988). Larger and aggregated convective cells have reduced evaporation associated with dry air entrainment (e.g., Jeevanjee & Zhou, 2022) and convective updraft merging (Glenn & Krueger, 2017) that may impact precipitation efficiency. These processes may have biased representation in CPMs. Past model evaluations suggest that CPMs overproduce the number of deep convective cores containing heavy rainfall (Yun et al., 2020) while reproducing the number and total rainfall of MCSs (Prein et al., 2017; Zhang et al., 2021). CPMs with kilometer-scale grid spacing also underestimate dry air entrainment (e.g., Bryan & Morrison, 2012) and produce overly wide convective updrafts and downdrafts (e.g., Varble et al., 2020).

Convective updrafts horizontally detrain heat, moisture, momentum, and condensate to promote stratiform anvil growth (Houze, 2004). Mesoscale updrafts and downdrafts associated with mid-level inflow in a sheared environment can promote stratiform rainfall enhancement (e.g., Chen & Frank, 1993), but condensate transport is still the primary source for stratiform growth (Gamache & Houze, 1983). Under-resolved and overly-wide and strong convective updrafts in km-scale models with excessive riming (e.g., Fan et al., 2017; Stanford et al., 2017; Varble et al., 2014a) may produce insufficient ice detrainment to stratiform regions which limits stratiform precipitation (Han et al., 2019; Varble et al., 2014b). Thus, CPM-overestimated convective contribution to rainfall might stem from coupled dynamical and microphysical processes.

The sensitivity of simulated convective cells and updrafts to model resolution has been investigated in many previous case studies using idealized and real case simulations (e.g., Bryan et al., 2003; Craig & Dörnbrack, 2008; Lebo & Morrison, 2015; Petch et al., 2002; Stanford et al., 2020; Wang et al., 2022). Bryan and Morrison (2012) found that convective rainfall and cell depth in a mid-latitude continental squall line decreased as horizontal grid spacing decreased from 4 km to 250 m, partially because convective updrafts entrained more mid-tropospheric dry air as resolution increased, though such changes are not systematic across all environments (e.g., Bryan et al., 2003; Morrison et al., 2015). Others have found that convective cell area decreases and convective cell number increases moving from 3-km to finer grid spacing with lesser changes for grid spacing below 200–250 m (Lebo & Morrison, 2015; Nicol et al., 2015; Stanford et al., 2024). Convective updraft strength increases moving from 4-km to 1-km grid spacing owing to decreasing vertical pressure gradient forces as updraft width decreases (Morrison, 2016; Stein et al., 2015). Further decreases in grid spacing to 250-m or less can result in weaker updrafts owing to increasing buoyancy dilution from dry air entrainment effects (e.g., Wang et al., 2020). These convective draft differences can also modulate vertical transport of zonal momentum that affects the convective system's evolution (Varble et al., 2020).

With regional weather and climate models already being run with 3–4 km grid spacing (e.g., Casaretto et al., 2021; Dowell et al., 2022), there is an urgent need to understand CPM biases and their causes to guide model improvement. This study leverages a warm season CPM simulation covering 15 October 2018 to 30 April 2019 with six case-focused simulations with grid spacing varying from 3 to 0.333 km. Measurements were collected from the Remote sensing of Electrification, Lightning, And Mesoscale/microscale Processes with Adaptive Ground Observations (RELAMPAGO; Nesbitt et al., 2021) and Clouds, Aerosols, and Complex Terrain Interactions (CACTI; Varble et al., 2021) field campaigns. A primary objective of the RELAMPAGO-CACTI

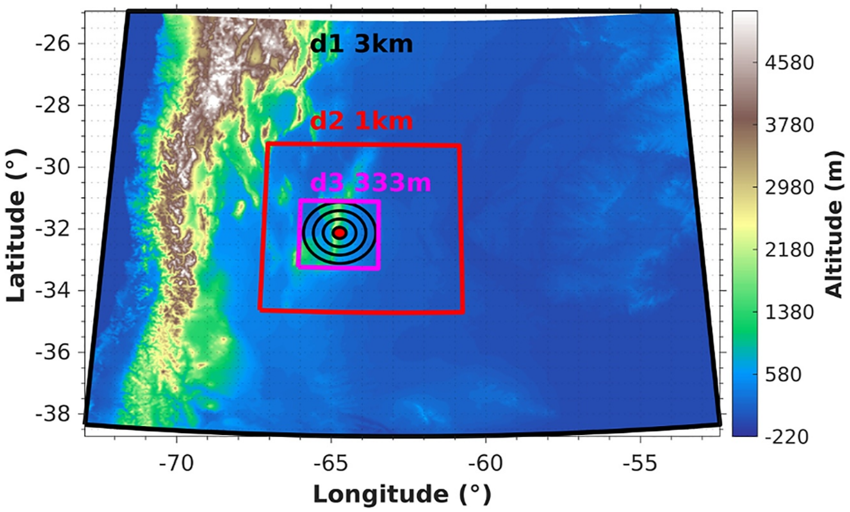

Figure 1. Model domains for conducting the multiscale simulations. The red dot represents the CSAPR2 radar location with 20-, 50-, 80-, and 110-km radar range rings in black.

campaign was to assess processes associated with deep convection initiation and upscale growth, using a location where storms frequently initiate and often rapidly grow over complex terrain. Consistent with this objective, this study uses radar-derived convective cell tracks to evaluate simulated convective cell growth including its contribution to convective and stratiform precipitation, as well as its sensitivity to convective instability and model resolution.

The remaining sections are organized as follows: Section 2 introduces the model setup, observed and simulated data sets, and methods for identifying and tracking convective and stratiform objects. Section 3 presents evaluation of domain-total convective and stratiform rainfall and their interactions. Section 4 analyzes simulated convective cell biases. Section 5 investigates convective updraft property contributions to cell biases. Section 6 focuses on the sensitivity of cell biases to model resolution. Finally, discussion and conclusions are presented in Section 7.

2. Data and Methodology

2.1. Observations

Our analyses focus on the Sierras de Córdoba (SDC) range (the mountain range cutting through d2 and d3 in Figure 1) in central Argentina, which is offset ~400 km east of the Andes. This region is moistened by the northerly South American low-level jet (Salio et al., 2002, 2007; Sasaki et al., 2022, 2024; Vera et al., 2006) under the influence of synoptic troughs (Piersante et al., 2021; Rocque & Rasmussen, 2022) and a surface low pressure in the lee of the Andes (Seluchi et al., 2003) that build convective instability beneath inversions and steep lapse rates caused by westerly flow over the Andes (Rasmussen & Houze, 2011, 2016; Ribeiro & Bosart, 2018; Schumacher et al., 2021). This meteorological setup interacts with the mountainous terrain (Lareau et al., 2024) to produce frequent deep convection initiation (Marquis et al., 2021, 2023; Nelson et al., 2021, 2022), rapid growth (Feng et al., 2022; Mulholland et al., 2018), and organization (Mulholland et al., 2019; Singh et al., 2022; Trapp et al., 2020) of deep convection, making it a prime location to study deep convective cloud processes. This led to the RELAMPAGO (Nesbitt et al., 2021) and CACTI (Varble et al., 2021) field campaigns being conducted in this area between October 2018 and April 2019.

A C-Band Scanning Atmospheric Radiation Measurement (ARM) Precipitation Radar (CSAPR2) was operated at the red dot location in Figure 1 about 20 km east of the primary SDC north-south ridgeline to measure precipitation properties over and downstream eastward of the mountainous terrain. The radar experienced downtime from 27 December 2018 to 20 January 2019, 9 February to 23 February 2019, and after 3 March 2019. Details on radar volume scans performed every 15 min are available in Feng et al. (2022).

CSAPR2 measurements (Hardin et al., 2018, 2024) are quality controlled with the Taranis radar processing software (Hardin, Bharadwaj, et al., 2020) that removes non-meteorological and second-trip echoes. Specific differential phase (K_{dp}) is used to correct for attenuation in radar reflectivity following Lim and Chandrasekar (2016) through a self-consistency algorithm with a hybrid K_{dp} retrieval using spline (Wang & Chandrasekar, 2009) and linear programming (Giangrande et al., 2013) techniques. Data were then re-gridded to Cartesian coordinates with Cressman weighting, a range-dependent radius of influence, and 500-m horizontal and vertical grid spacing using the Python ARM Radar Toolkit (Helmus & Collis, 2016). Rain rates are retrieved using a blended rain rate estimator combines multiple individual rain rate estimators using reflectivity, differential reflectivity, and K_{dp} through a decision tree (Cifelli et al., 2011; Ryzhkov et al., 2005). Estimator coefficients are tuned based on T-Matrix scattering calculations applied to Parsivel disdrometer data collected at the observing site (Hardin, Giangrande, & Zhou, 2020). Radar reflectivity in linear units and rain rates are then averaged to 3-km horizontal grid spacing to match model output. We validate the radar-retrieved rain rate using RELAMPAGO-CACTI tipping bucket rain gauge measurements (Kyrouac et al., 2018) taken at the same radar location (Figure S1 in Supporting Information S1). The radar-retrieved rainfall closely matches that recorded by the rain gauge, with some discrepancies in heavier rains. Some differences are expected, as the radar-retrieved rain rates represent an average over a 3-km grid at a specific time every 15 min, whereas the tipping bucket rain gauge measures the rainfall continuously over a time period at a point location.

The processed CSAPR2 data set is used to analyze convective-stratiform rainfall partitioning and convective cell life cycles. Every 15-min Top-Of-Atmosphere (TOA) infrared (IR) brightness temperature (T_b) measurement at 2-km grid spacing (Smith & Thieman 2019; Varble et al., 2024) from Geostationary Operational Environmental Satellite 16 (GOES-16) is matched to radar-tracked convective cells (see Section 2.3 for tracking details). Environmental conditions are derived from the Interpolated Sonde (INTERPSONDE) product (Fairless & Giangrande, 2018). INTERPSONDE temporally interpolates radiosondes with scaling of the moisture profiles to continuous precipitable water measurements collected by a microwave radiometer. Inputted radiosondes were launched every 3–4 hr at the CSAPR2 site between 12 and 00 UTC (9–21 LT) to quantify CAPE. These derived CAPE values are matched in time with each convective cell's initiation time. All convective cells occur within the 110-km radar range from the ARM sounding site. Varble et al. (2024) show that the ARM site reproduces structural differences between shallow and deep cell thermodynamic profiles at CI locations in the weather research and forecasting (WRF) simulation for both narrow and wide cells when averaged over the full data sets used here.

2.2. Simulations

A convection-permitting simulation covering 15 October 2018 to 30 April 2019 was conducted using the weather research and forecasting (Skamarock et al., 2019) model version 4.1.1 with 15-min output that matches the observed radar volume frequency. The model was initialized at the start of the field campaign on 15 October 2018, with boundary conditions updated every 6 hr. Initial and boundary conditions were sourced from the ECMWF ERA-5 reanalysis (Copernicus Climate Change Service, 2017). For more details on the model setup, please refer to Zhang et al. (2021). Its domain (d2) is shown in Figure 1. The simulation is performed at 3-km horizontal grid spacing with 80 vertical levels preferentially stacked below 5-km altitude but with all layer thicknesses less than 500 m. Microphysical processes are parameterized using the Thompson aerosol aware scheme (Thompson & Eidhammer, 2014), planetary boundary layer (PBL) processes are parameterized using the Mellor-Yamada Nakanishi Niino (Nakanishi & Niino, 2006, 2009) eddy diffusivity mass flux scheme, the surface layer is parameterized by the Eta similarity scheme (Janjic, 2002), and radiation is parameterized by the RRTMG shortwave and longwave schemes (Iacono et al., 2008). These physics parameterization schemes are similar to those used in the operational 3-km high resolution rapid refresh (HRRR) model run over the U.S. (Dowell et al., 2022), with an aim of providing insights that could potentially improve operational weather forecasting.

The simulated rain rate is derived by multiplying the rainwater content by the mass-weighted fall speed for rain at 2.5 km above mean sea level (AMSL) for comparisons with 2.5 km AMSL radar-retrieved rain rates that avoid ground clutter and variable lowest radar beam heights with range while remaining below the melting level. Contributions of graupel and hail to precipitation are ignored in simulations to be consistent with radar retrievals.

In addition to the season-long simulation, two convective cases were selected for higher resolution simulations (Table 1), one under low CAPE conditions (<300 J kg^{-1}) and one under high CAPE conditions (>1000 J kg^{-1}).

Table 1
Case Study Simulation Time Periods

Experiments	Domains	Analysis periods	d1 restart	d2 initialization	d3 initialization
Low CAPE 3 km	d1	00–12Z, 26 Nov	12Z, 25 Nov	N/A	N/A
Low CAPE 1 km	d1, d2	00–12Z 26 Nov	12Z, 25 Nov	12:15Z, 25 Nov	N/A
Low CAPE 333 m	d1, d2, d3	00–12Z 26 Nov	12Z, 25 Nov	12:15Z, 25 Nov	18:15Z, 25 Nov
High CAPE 3 km	d1	16Z, 10 Nov–6Z, 11 Nov	12Z, 09 Nov	N/A	N/A
High CAPE 1 km	d1, d2	16Z, 10 Nov–6Z, 11 Nov	12Z, 09 Nov	4:15Z, 10 Nov	N/A
High CAPE 333 m	d1, d2, d3	16Z, 10 Nov–6Z, 11 Nov	12Z, 09 Nov	4:15Z, 10 Nov	10:15Z, 10, Nov

These cases were chosen based on their convective cell and convective-stratiform rainfall partitioning statistics being somewhat similar to the overall low and high CAPE convection statistics in the full 6.5-month run and are limited in length due to the computational expense of the highest resolution domain. There are 3 simulations performed for each case, one with only d1, a second with d2 nested into d1, and a third with d3 nested into d2 and d1 (Figure 2). Two-way nesting is employed. These simulations are restarted from the seasonal simulation using a 12 UTC (9 LT) restart file prior to the start of the event. The nested inner domains (d2 and d3) are delayed in their starts and allowed to spin up for 11.75 and 5.75 hr, respectively. Exact restart, initiation, and analysis times are listed in Table 1. The total simulated hours including model spin up are 24 hr for the 3 low CAPE period runs and 30 hr for the 3 high CAPE period runs. The full CSAPR2 coverage area (110 km range) is encapsulated by d3 (Figure S2 in Supporting Information S1). All three domains share the same vertical levels and physics parameterizations as the seasonal run, except in d3, where the planetary boundary layer scheme is turned off. With a 0.333 km grid spacing in d3, the assumptions made in the boundary layer scheme are violated, so diffusion is computed using a prognostic equation for the 1.5-order turbulent kinetic energy closure (Bretherton & Park, 2009).

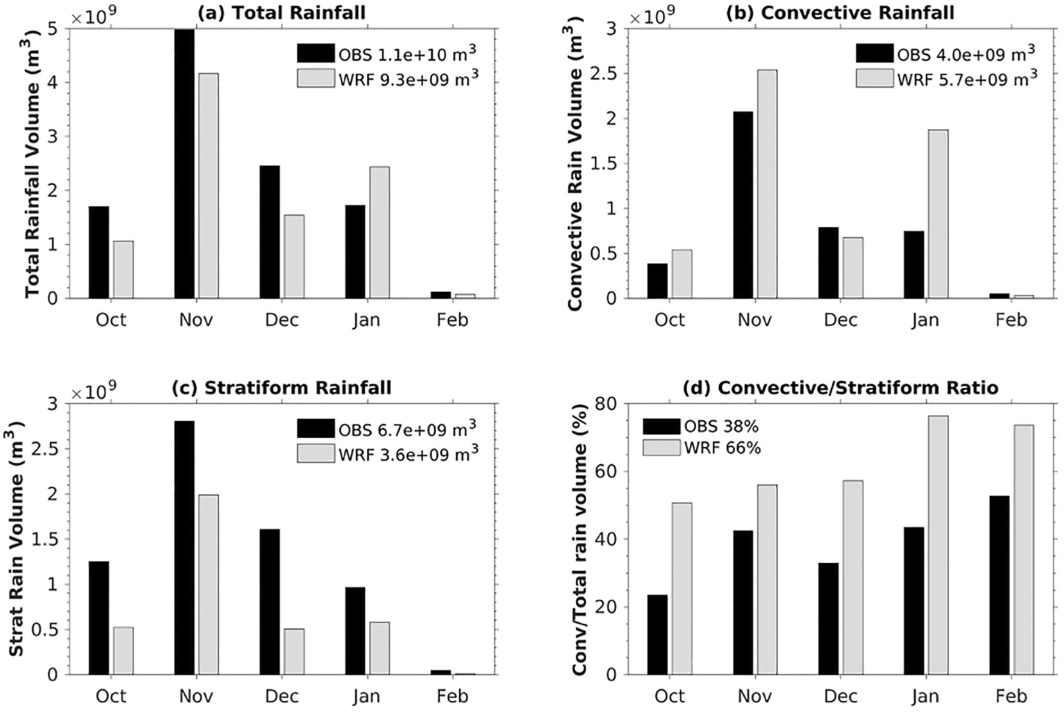

Figure 2. Volume of (a) total, (b) convective, and (c) stratiform rainfall, as well as (d) convective/stratiform rainfall ratio by month with totals over all times shown in the legends.

2.3. Convective Cell Tracking

Convective cells evolve rapidly, can propagate quickly, and are often connected by light rain, making them difficult to define and track. This study altered the convective region tracking method in the open-source PyFLEXTRKR algorithm (Feng, Hardin, et al., 2023). 15-minute composite (column maximum) reflectivity maps, derived from both WRF simulations and CSAPR2 observations, are used to consistently define and track observed and simulated convective cells using the open-source PyFLEXTRKR algorithm. Note that because cells require a composite reflectivity of at least 10 dBZ, light precipitation in the column is required for cell identification. The melting layer was designed to avoid cell identifications associated with high melting level reflectivity (Feng et al., 2022). The CSAPR2 reflectivity measurements at native 500-m grid spacing, and the higher resolution simulations with 0.333-km and 1-km horizontal grid spacing, are conservatively coarsened to 3-km horizontal grid spacing by averaging reflectivity in linear units ($mm^6\ m^{-3}$) and then converting to $\log_{10}$ (dBZ) units. Terrain blockage of CSAPR2 radar beams is analyzed with a digital elevation map using the wradlib (Heistermann et al., 2013) Python package. The same beam blockage mask is applied to the WRF output to have consistent observing volumes with measurements. Dates and times in which the CSAPR2 did not obtain PPI volumes were also removed in the WRF data set.

Following the method in Steiner et al. (1995), the tracking algorithm identifies convective cores using the horizontal texture of composite reflectivity by defining the peakedness of each point, which is the difference between each grid point reflectivity (Z_{grid}) and the surrounding background reflectivity (Z_{bkg}). Z_{bkg} is defined using averaged values within a 13.5-km radius from each 3-km spacing grid point. A grid point is classified as a convective core if the reflectivity peakedness ($Z_{\mathrm{grid}} - Z_{\mathrm{bkg}}$) is higher than the reflectivity-dependent threshold equal to $10\cos(\pi Z_{\mathrm{bkg}}/120)$ or if Z_{grid} exceeds 55 dBZ. To avoid over-segmentation, identified convective cores are further expanded with a Z_{bkg}-dependent dilation radius (R_{core}) defined by Equation 1 where $\mathrm{R_{core}}$ has units of km and $\mathrm{Z_{bkg}}$ has units of dBZ:

$$R_{\mathrm{core}} = \min\left[\max\left(3 + 0.5\left\lceil\frac{Z_{\mathrm{bkg}} - 25}{5}\right\rceil, 3\right), 5\right] \tag{1}$$

5 km is set as the maximum dilation radius to avoid grouping of too many convective cores into one object. Core grid points adjoining one another are merged into individual core objects. Core objects are then horizontally expanded 1 km at a time until they reach another object or 7 km distance from the core. When they meet another object, they are not merged with it. This expanded mask around cores encapsulates cells and is applied to more easily track cells via overlap between the time gap of 15 min. Examples of identified convective cell masks in observations and the 3-km simulation are shown with black contours in Figure S2 in Supporting Information S1. These convective cells are tracked based on their spatial overlapping masks exceeding 30% between consecutive timesteps, producing track trajectories like those shown by black lines in Figure S2 in Supporting Information S1. Convective cell advection is estimated using the cross-correlation of reflectivity between consecutive timesteps and applied to increase the overlapping cell masks between timesteps. The minimum core area for tracking after dilation is five pixels with an area of 45 km^2.

A convective cell is identified as a merger if two or more separate cells at the current timestep overlap with a single cell by more than 30% in the subsequent timestep. The largest cell at the current timestep is then continuously tracked forward while the smaller cell tracks are terminated and marked as mergers. Similarly, a cell is identified as a split if a single cell at the current timestep overlaps with two or more cells by more than 30% at the next time step. The smaller cells are marked as splits that can be differentiated from isolated initiation. While this 30% overlap threshold was carefully calibrated in Feng et al. (2022) for the cell advection and 15-min time step to yield results consistent with subjective visual tracking of cells and to avoid excessive merging and splitting identification given their uncertainty, different numbers of cells, mergers, and splits would be expected with a temporal resolution finer than 15 min with a potentially different optimal overlap threshold. Additional tracking details are described in Feng et al. (2022).

In addition to cell tracking for 3-km horizontal grid spacing, a similar algorithm is applied to the CSAPR2 500-m, WRF 1-km, and WRF 0.333-km native grids for obtaining higher-resolution cell tracks. To adapt the tracking to finer grid spacings, the 1-km cell tracking uses a similar core dilation radius as described by Equation 1 but with an adjusted minimum dilation from 3 to 2 km. The 0.5-km and 0.333-km cell tracking use 1-km minimum core

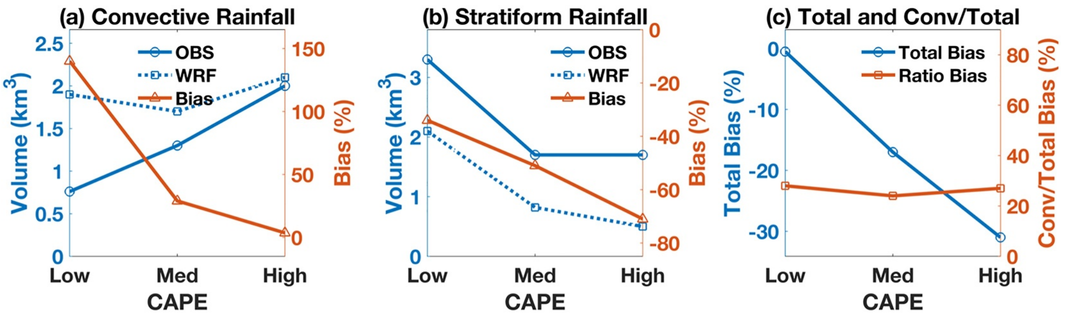

Figure 3. (a) Convective and (b) stratiform rainfall in observations and simulations with model relative biases as a function of CAPE. (c) Total rainfall relative biases and convective contribution to total rainfall absolute biases conditioned by CAPE.

dilation with a minimum core area adjusted from 45 to 13 km^2. The radius of the region for computing background reflectivity is also reduced from 13.5 to 11 km in 1-km and 0.333-km settings. In addition, the core expansion into a cell mask is limited to 5 km in these higher resolution runs.

All convective cell statistics are computed within their cell masks. Cell areas are defined by the area within the cell masks (black contours in Figure S2 in Supporting Information S1) where the composite reflectivity is greater than 10 dBZ. Echo Top Height (ETH) is estimated for each convective cell using the highest altitude where reflectivity exceeds 10 dBZ within the convective cell masks. Convective area and ETH are calculated throughout the lifecycle of convective cell tracks. Cell track initiation times are matched with the INTERPSONDE and simulated observing site vertical profile derived environmental conditions at that time. We focus on the most unstable CAPE (MUCAPE, simplified as CAPE hereafter), which is the CAPE associated with the parcel lifted from the level with the maximum equivalent potential temperature in the lower troposphere. The CAPE calculation assumes reversible ascent with condensate retained as the parcel rises without considering fusion contributions to latent heating. The time evolution of CAPE at the CSAPR2 radar location is well reproduced by the season-long simulation, as shown in Zhang et al. (2021).

3. Simulated Rainfall Evaluation

All rainfall analyses use rain rates estimated from a scanning precipitation radar for observations rather than rain gauge measurements. The temporal evolution of WRF-simulated rainfall in d3 follows that of estimated rainfall from the CSAPR2 radar (Figure S3a in Supporting Information S1), with perhaps a few subtle distinctions. The cumulative rainfall is slightly underestimated by the simulation (Figure S3b in Supporting Information S1) but within the ∼15% underestimation that is within the uncertainty expected from blended polarimetric C-band radar rain retrievals in past studies (e.g., Cifelli et al., 2011; Giangrande et al., 2014). The simulation also reproduces the general month-to-month variations in rainfall (Figure 2a).

Convective and stratiform rainfall are retrieved from the 2.5-km altitude simulated and CSAPR2 retrieved rain rates with convective rainfall defined as rain rates within convective cell masks and the rain rates outside convective cell masks defined as stratiform rainfall. However, dividing the total rainfall into convective and stratiform contributions highlights more significant model biases. The WRF simulation overestimates the convective rainfall by 43% (Figure 2b) while underestimating the stratiform rainfall by 46% (Figure 2c). Thus, the simulated convective to stratiform rainfall volume ratio (66%) is much greater than observed (38%).

The simulated convective and stratiform rainfall biases are sensitive to CAPE conditions (Figure 3). The simulated overestimation of convective rainfall decreases as CAPE increases (Figure 3a), while simulated underestimation of stratiform rainfall increases (Figure 3b). Total rainfall is well predicted in low CAPE conditions but becomes increasingly underpredicted as CAPE increases (blue line in Figure 3c). Interestingly, bias in the ratio of convective to total rainfall is not sensitive to CAPE with simulations overestimating the convective contribution by 24%–28% (orange line in Figure 3c). These values reflect a similar shift to more convective rainfall as CAPE increases in both simulations and observations; however, the simulations have much greater contributions to total rainfall from convective regions for all CAPE conditions.

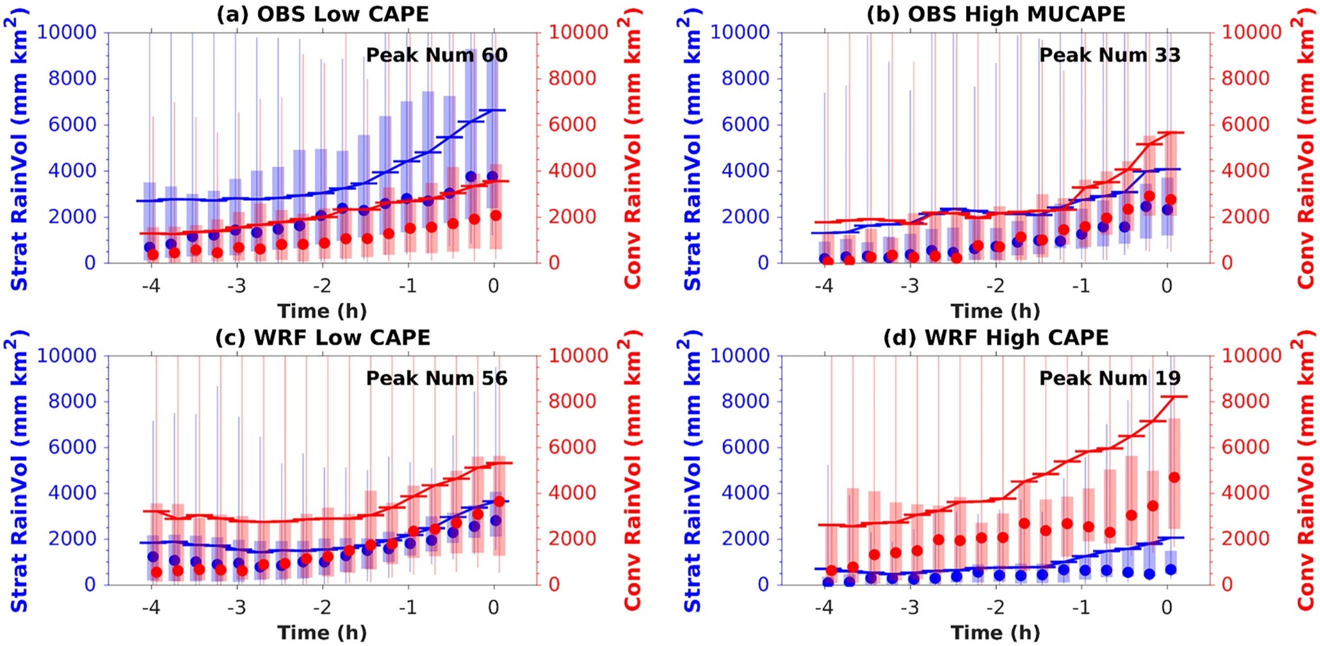

Figure 4. Stratiform and convective rainfall volume in the 4 hr leading up to the peak rainfall volume in the domain at time 0 for peak volumes that exceed 2,000 mm km^2. (a–b) Observed and (c–d) simulated time series are shown for (a, c) low and (b, d) high CAPE conditions. Medians and means are represented by circles and horizontal lines, respectively. Interquartile and 5th to 95th ranges are shown by the bars and vertical lines, respectively.

Stratiform rainfall volume generally increases with convective rainfall volume (Figure S4 in Supporting Information S1). Their correlation coefficients are between 0.66 and 0.91 depending on CAPE conditions and whether observations or simulations are considered. The correlation coefficients in observations (Figures S4a and S4c in Supporting Information S1) are lower than those in WRF (Figures S4b and S4d in Supporting Information S1) because observed stratiform rainfall has a large range when convective rainfall is less than 10,000 mm km^2 with some very large values that are not reproduced in WRF. Even neglecting those values, the observed linear regression slopes are greater than simulated suggesting the model requires more convective rainfall than is observed to yield a similar amount of stratiform rainfall. The regression slopes in higher CAPE conditions are also less than those in lower CAPE conditions by about a factor of 2, meaning high CAPE storms tend to form less stratiform rainfall than low CAPE storms for a given amount of convective rainfall. This effect is captured by the simulation and might relate to more intense updrafts in higher CAPE conditions that produce more fast-falling rimed ice, less snow detrainment, and higher altitude anvils that accentuate sublimation relative to lower CAPE conditions. All of these processes would slow the development of robust stratiform precipitation, and such processes may be exaggerated in the simulations relative to the observations.

The correlation between convective and stratiform rainfall can also be tracked in time to assess convective and stratiform interactions. The simulation produces a similar number of rainfall volume peaks >2,000 mm km^2 to observed in lower CAPE conditions (56 vs. 60; Figures 4a and 4c) but underestimates the number of peaks in higher CAPE conditions (19 vs. 32; Figures 4b and 4d). For lower CAPE, observed stratiform rainfall is always greater than convective rainfall and grows at a faster rate than convective rainfall within 2 hr of peak total rainfall (Figure 4a). In contrast, the simulated stratiform rain volume remains lower than the convective rain volume with a growth rate that is similar or even slightly lesser than the convective growth rate (Figure 4b). Higher CAPE, on the other hand, facilitates more rapid convective growth than stratiform growth in observations. The simulation reproduces this effect but with much greater convective precipitation and much lesser stratiform precipitation (Figures 4b and 4d). This again demonstrates that the simulation can qualitatively capture the response of convective-stratiform rainfall ratio to CAPE but is unable to predict its absolute magnitude across CAPE conditions with a bias that is present throughout the entire growth stage of MCSs.

To assess how convective cells contribute to WRF overproduced convective rainfall, Figure 5 shows convective rainfall separated by small (<300 km^2), medium (300–550 km^2), and large (>550 km^2) cells and simulated biases

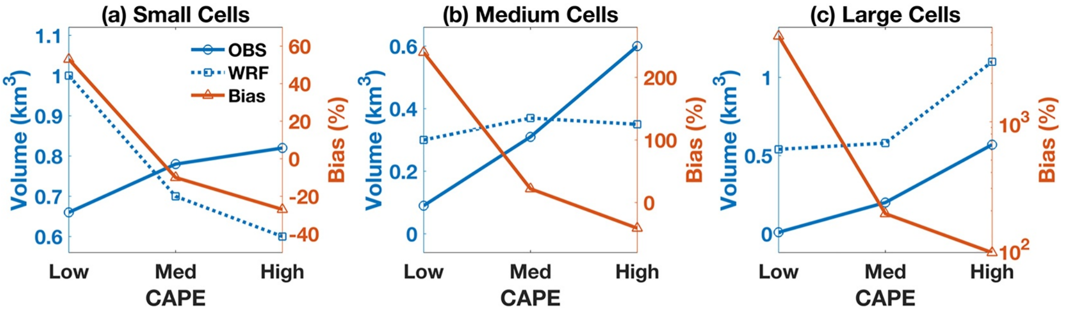

Figure 5. Cumulative (a) small, (b) medium, and (c) large convective cell rainfall volumes for observations and WRF with relative biases in WRF, conditioned by CAPE.

relative to observations. Rainfall produced by small cells is overestimated by the model in low CAPE conditions and underestimated in medium and high CAPE conditions. Medium-sized cell rainfall is overestimated by the model in low and medium CAPE and underestimated in high CAPE. Finally, large cell rainfall is overestimated by the model in all CAPE conditions. These findings align with cell number biases shown in Section 4, biases that are investigated further in Sections 4-6.

For all cell sizes, the observed convective rainfall increases as CAPE increases. However, this is only true for large cells in simulations, and simulated small cell rainfall decreases as CAPE increases. In low CAPE scenarios, all cell sizes contribute to overestimated convective rainfall; whereas in medium and high CAPE scenarios, the larger cells produce overestimated total convective rainfall. Furthermore, model bias increases as cell sizes grow. Clearly, cell properties change differently as a function of CAPE in observations and the simulation. Simulated convective cell biases are further evaluated in Section 4 to reveal potential causes of this difference.

4. Simulated Convective Cell Evaluation

There are 5,662 observed and 14,299 simulated convective cells that are tracked; thus, the model produces ~2.5 times more cells than are observed. An overestimation of cell number in 3–4 km horizontal grid spacing models with the Thompson scheme including HRRR has been noted previously (Clark et al., 2014; Duda & Turner, 2021, 2023), though such a large bias is not seen for the number of convective systems using reflectivity-based objects (e.g., Grim et al., 2021). 2,355 observed and 6,016 simulated convective cells initiate and grow (by reflectivity area) within the domain, and these are used in further analyses. The simulation reproduces the spatial distribution of these cells, with the highest frequency centered over the SDC range just east of the highest ridgeline (Figure 6). The eastward propagation of these cells is also captured by the simulation, suggesting that it reasonably captures the processes controlling the spatiotemporal distribution of moist convection despite more numerous cells that may thus be the result of convective scale processes.

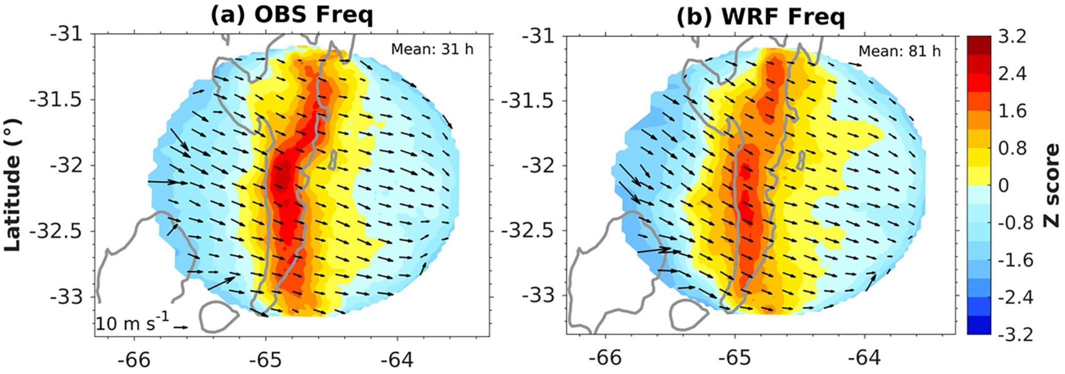

Figure 6. Spatial occurrence (color fills) and propagation (vector) of (a) observed and (b) simulated convective cell tracks. The Z score is the domain-normalized number of cell hours at a point. Gray contours represent the 1-km terrain height AMSL.

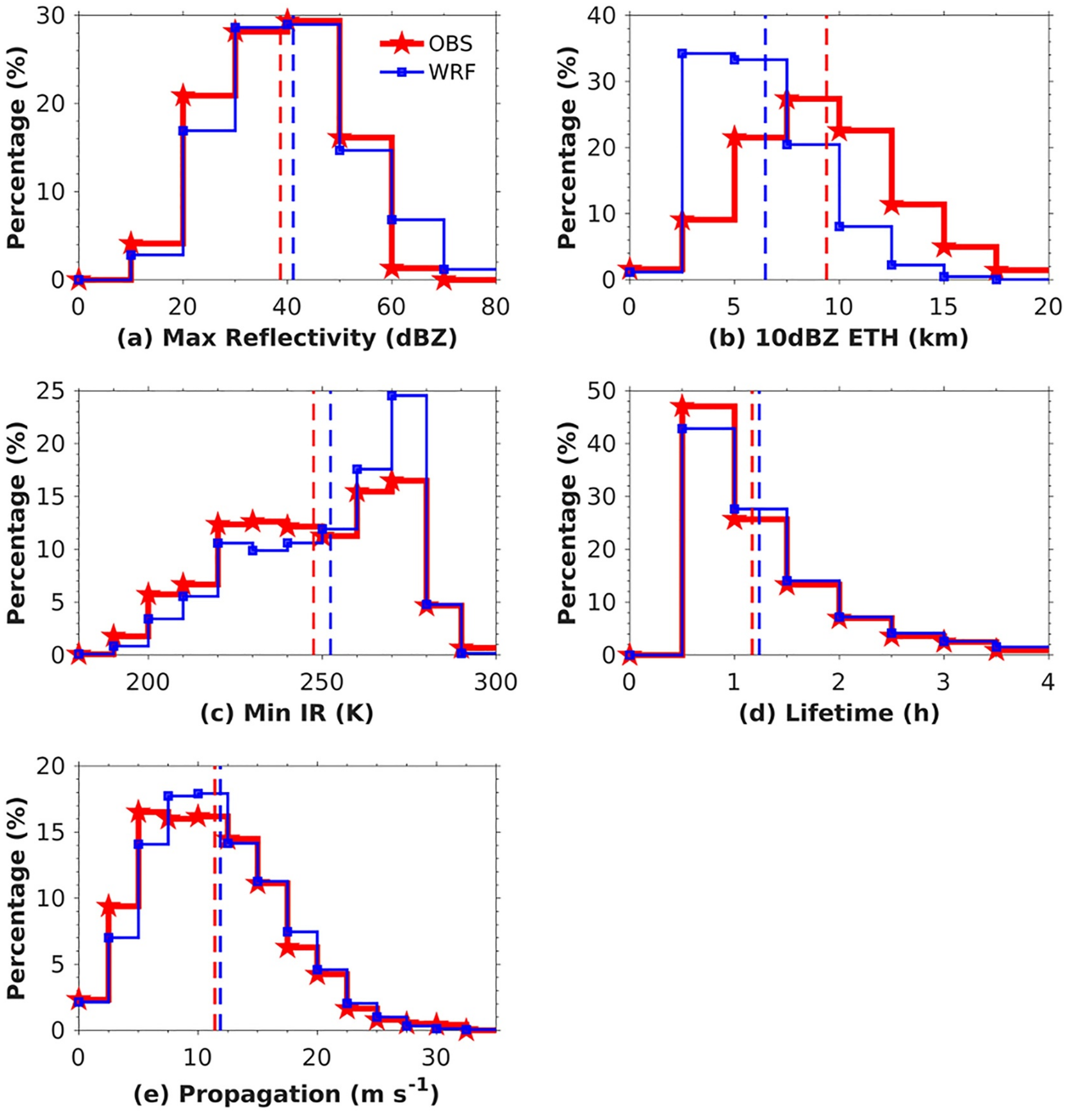

Figure 7. PDFs of convective cell (a) lifecycle-maximum reflectivity, (b) 10-dBZ ETH, (c) lifecycle-minimum TOA IR T_b, (d) lifetime, and (e) propagation speed. Red and blue dashed vertical lines represent the mean values in observations and simulations, respectively.

The simulation also generally captures the peak probabilities of convective cell maximum reflectivity, lifetime, and propagation speed (Figures 7a–7d and 7e), though with a slight bias toward greater values. The greater occurrence of simulated reflectivities exceeding 60 dBZ could be related to the observed reflectivities being C-band in which large hydrometeors such as hail can produce non-Rayleigh scattering, whereas WRF reflectivities are estimated assuming purely Rayleigh scattering. The reflectivity difference is unsurprising based on previous studies (e.g., Varble et al., 2011). Differences between observation and simulation mean values are more substantial for ETH (Figure 7b). The model overestimates the probability of shallow convective cells (ETH = 2.5–7.5 km) and underestimates the probability of deep convection (maximum ETH > 7.5 km). Part of this difference is attributed to non-uniform beam filling and extrapolation artifacts in the radius of influence Cartesian gridding of observations, leading to a high bias in ETH, as shown in Varble et al. (2024). Nonetheless, this is not the sole reason for WRF's excessive frequency of shallow 10-dBZ ETH, as its distribution is more positive skewed than the observed distribution. Indeed, Figure 7c shows that the model overestimates the probability of cells with warmer TOA IR T_b compared to observations. Despite limitations of TOA IR T_b, such as anvil clouds obscuring shallow cells, it complements the ETH analysis by offering a more reliable measure of cloud top height for deep

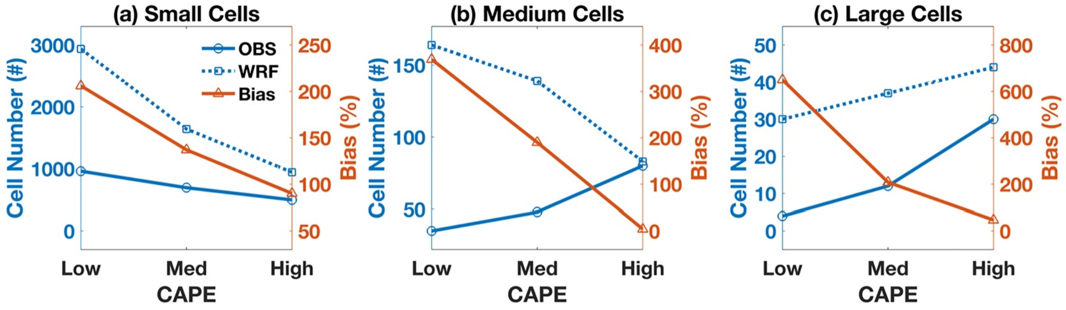

Figure 8. Observed and simulated (a) small, (b) medium, and (c) large convective cell track numbers and WRF biases relative to observed, conditioned by CAPE.

cells. In summary, both ETH and TOA IR T_b consistently reveal that the model underestimates the probability of shallow cells.

The high bias in simulated cell number is most apparent in low CAPE conditions for all cell areas and decreases as CAPE increases (Figure 8). However, the model produces more numerous convective cells across all CAPE conditions for all convective cell areas. The cell number bias also increases with the cell area in low CAPE conditions. However, in high CAPE conditions, the WRF overestimation of cell number decreases from small to medium area cells and increases from medium to large cells. This indicates potentially different process controls on cell size distributions in high CAPE relative to low CAPE conditions.

In addition to convective cell number, the convective cell area differences between the simulation and observations vary by CAPE. Simulated convective cell areas are larger than observed in low-medium CAPE conditions but the probability of large convective cells in high CAPE conditions is underestimated (Figure S5 in Supporting Information S1). Recall that the model overestimation of total convective rainfall decreases with CAPE, partially a result of the model overestimation of convective cell number decreasing with CAPE (particularly for large cells that produce the heaviest rainfall). The change in convective rainfall volume biases as cell area changes also far exceeds the change in convective cell number biases (Figure 5 vs. Figure 8).

Given the differences in observed and simulated cell properties, convective cell net growth is explored for the lifecycle growth period between the cell initiation and the lifecycle maximum cell area times. Net growth during this lifecycle period is controlled by convective cell expanding, shrinking, merging, and splitting processes, which are quantified and evaluated in Figure 9. Merging and splitting areas are the cell area difference between the two consecutive timesteps over which merging or splitting occurs and includes the potential shrinking and expansion during that period. A pure split occurs when a cell divides from its parent cell over two consecutive timesteps without any other cell interactions. We found that a pure split is uncommon in both the observations and simulation, splits are combined with splits plus mergers occurring at the same time into an "other" category.

The mean and interquartile range values of the simulated small cell net growth are greater than observed. Observed and simulated cell expansion contributions to cell growth are both near 100% on average, with fewer contributions from shrinking, merging, and splitting. This indicates that small cell expansion growth dominates the observation-simulation net growth difference. However, medium area cell growth (Figure 9b) is underestimated by the model. Simulated medium area cell shrinking is slightly underestimated and the simulated merging is slightly greater than observed, but these are not able to counteract the dominant control of cell expansion, which is greater in observations. The mean and median simulated large cell net growth and expansion are similar to observed (Figure 9c), which is the result of combined overestimated expansion and underestimated merging in the simulation. Thus, despite differences in observed and simulated cell numbers, areas, and contributions to rainfall, there are limited differences in cell area growth lifecycles.

5. Physical Controls on Convective Cell Biases

Convective updraft area is calculated throughout each individual convective cell lifecycle in the simulation. Updraft regions are defined as having vertical velocity greater than 2 m s^{-1} and radar reflectivity greater than 10 dBZ within the identified convective cell footprints. Figure 10 shows that the lifecycle- and column-maximum

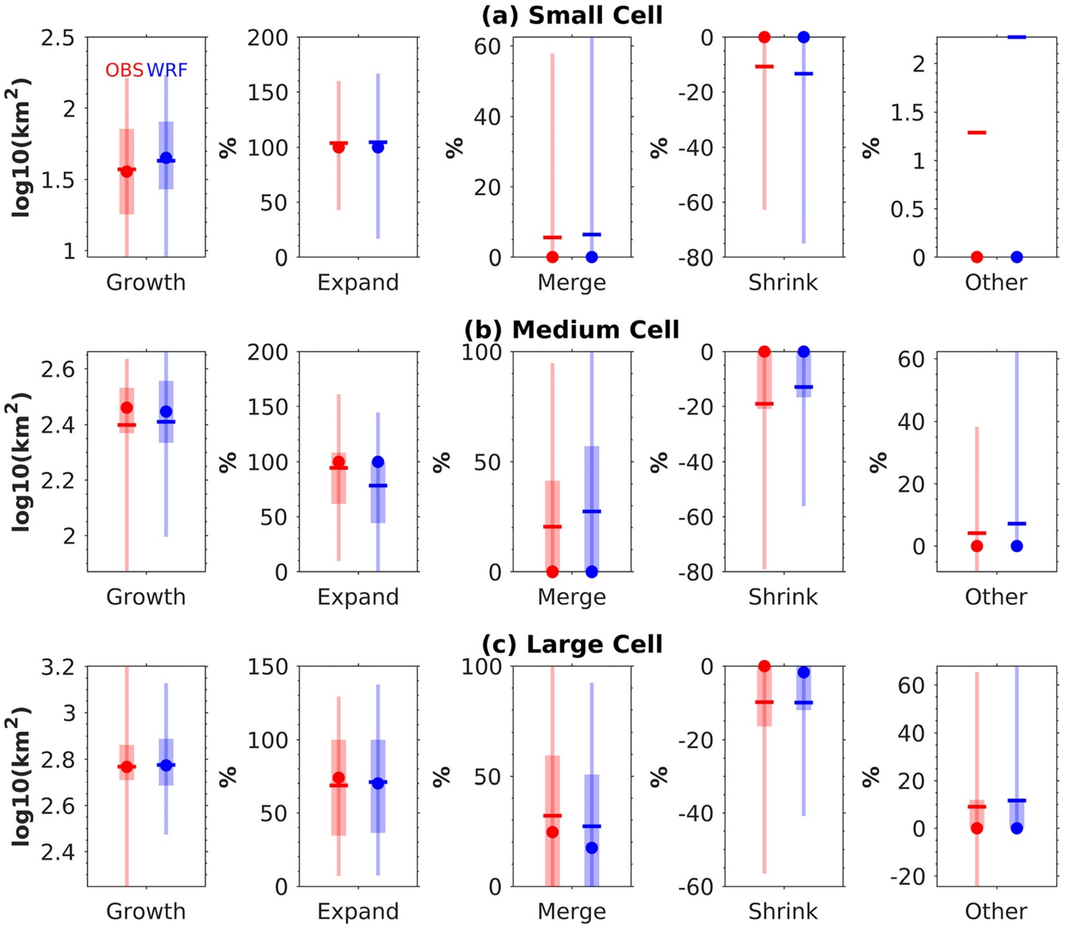

Figure 9. Observed (red) and simulated (blue) convective cell area net growth with contributions from cell expansion, merging, shrinking, and other (splitting, splitting plus merging) during the growth period between initiation and lifetime-maximum area across all CAPE conditions. Means and medians are represented by circles and horizontal lines, respectively. Interquartile and 5th to 95th ranges are shown by bars and vertical lines, respectively.

convective updraft area positively correlates with the lifecycle-maximum aggregated convective cell area with a linear correlation coefficient higher than 0.9 ($r = 0.85$–0.96 for 200,000 times of random bootstrapping), indicating a robust positive correlation. The maximum convective cell area reached is usually twice the column-maximum updraft area reached during a cell's lifecycle, though this ratio is sensitive to the definition of the updraft and cell area.

Relationships of the lifecycle-maximum convective cell circle-equivalent diameter ($2\sqrt{\mathrm{Area}/\pi}$) with the lifecycle-maximum 10-dBZ radar reflectivity ETH and lifecycle-minimum TOA IR T_b can inform potential observed and simulated updraft differences. In Figure 11, the highest observed ETHs reach 22 km, which is higher than those simulated, which reach 18 km, consistent with Figure 7b. The simulated linear regression slope between cell diameter and ETH (0.38) is lower than observed (0.52), indicating cells reach greater depths for a given cell area in observations as compared to the simulation.

Due to Cartesian gridding artifacts, non-uniform radar beam filling, and sidelobe contamination, the ETH estimated from ground-based radar measurements tends to be biased high (e.g., Lakshmanan et al., 2013), which likely contributes to the model-observation ETH difference. The TOA IR T_b measured by GOES-16 is re-gridded to WRF 3-km grids for comparison with simulated TOA IR T_b empirically derived from the simulated outgoing longwave radiation, following the approach in Yang and Slingo (2001). Higher TOA IR T_b indicates that the cloud top has more outgoing longwave radiation, which corresponds to a lower, warmer cloud top. The simulated lifecycle-minimum TOA IR T_b range of values agrees with that observed, but the absolute value of the regression

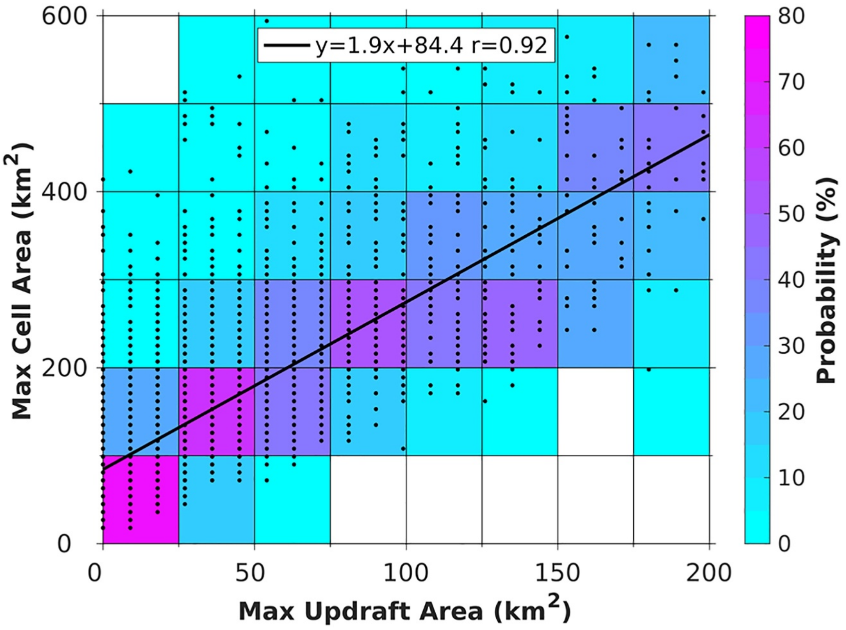

Figure 10. Lifecycle-maximum convective cell area as a function of lifecycle- and column-maximum updraft area. The color fill shows cell area PDFs conditioned on maximum updraft area, that is, within each maximum updraft area bin.

slope in the simulation is slightly less steep than observed (Figures 11c and 11d). That means for a given cell diameter, the simulation is more likely to have a lower cloud top than observed. This agrees with the radar ETH bias as a function of cell diameter, but with a much smaller difference, suggesting that a significant portion but not all the radar ETH difference is a retrieval artifact.

These relationships of convective updraft and cell properties suggest that convective cell area is a good qualitative proxy for updraft area and depth in the simulation. Although updraft properties are not directly retrievable from observations, it is physically plausible that observed cell area and depth also scale with updraft area (though potentially with a different slope). It is also plausible that the widest deepest updrafts exist in relatively high CAPE conditions. Figure S6 in Supporting Information S1 further demonstrates that the convective updraft area and cell depth increase as CAPE increases. This suggests that updraft widths would be least resolved in simulated low CAPE conditions, which is indeed where the largest model biases are found.

Excessive numbers of shallow cells in the simulation bring the average cell depth down for a given cell width, which may negatively impact stratiform rainfall formation. Convective cells that do not reach well above the freezing level likely have limited ice detrainment that is critical to the formation of stratiform anvil regions, and the simulation has excessive numbers of these cells. It is also possible that the deep cells in the simulation fail to detrain vapor-grown ice in sufficient amounts over sufficient height layers to adequately grow precipitating stratiform regions as highlighted in previous studies (Han et al., 2019; Varble et al., 2014b). In this scenario, underproduced stratiform precipitation in the simulation results in less extensive atmospheric stabilization caused by its upper level latent heating over lower level latent cooling. Such a process would leave more atmospheric instability to be consumed by additional convective cells. Thus, there could exist a positive feedback between the convective cell and stratiform biases, and such interactions deserve further investigation in the future.

Additional possible causes for excessive numbers of shallow convective cells are biased dynamical and/or microphysical processes. Focusing on possible dynamical biases, convective updrafts are severely under-resolved for 3-km horizontal model grid spacing, resulting in wider simulated updrafts than those in the real world. For relatively shallow cells with small areal coverage, updrafts are thinnest and thus potentially the most biased too wide, which could suppress entrainment dilution but enhance opposing vertical pressure gradients. The minimum resolved wavelength by WRF is approximately 7 times the grid spacing (Skamarock, 2004). Thus, despite explicit convection, this simulation at 3-km grid spacing only fully resolves a half wavelength feature like a convective updraft if it is 10.5 km or more wide, corresponding to a circular convective updraft area of 87 km^2 and a cell area

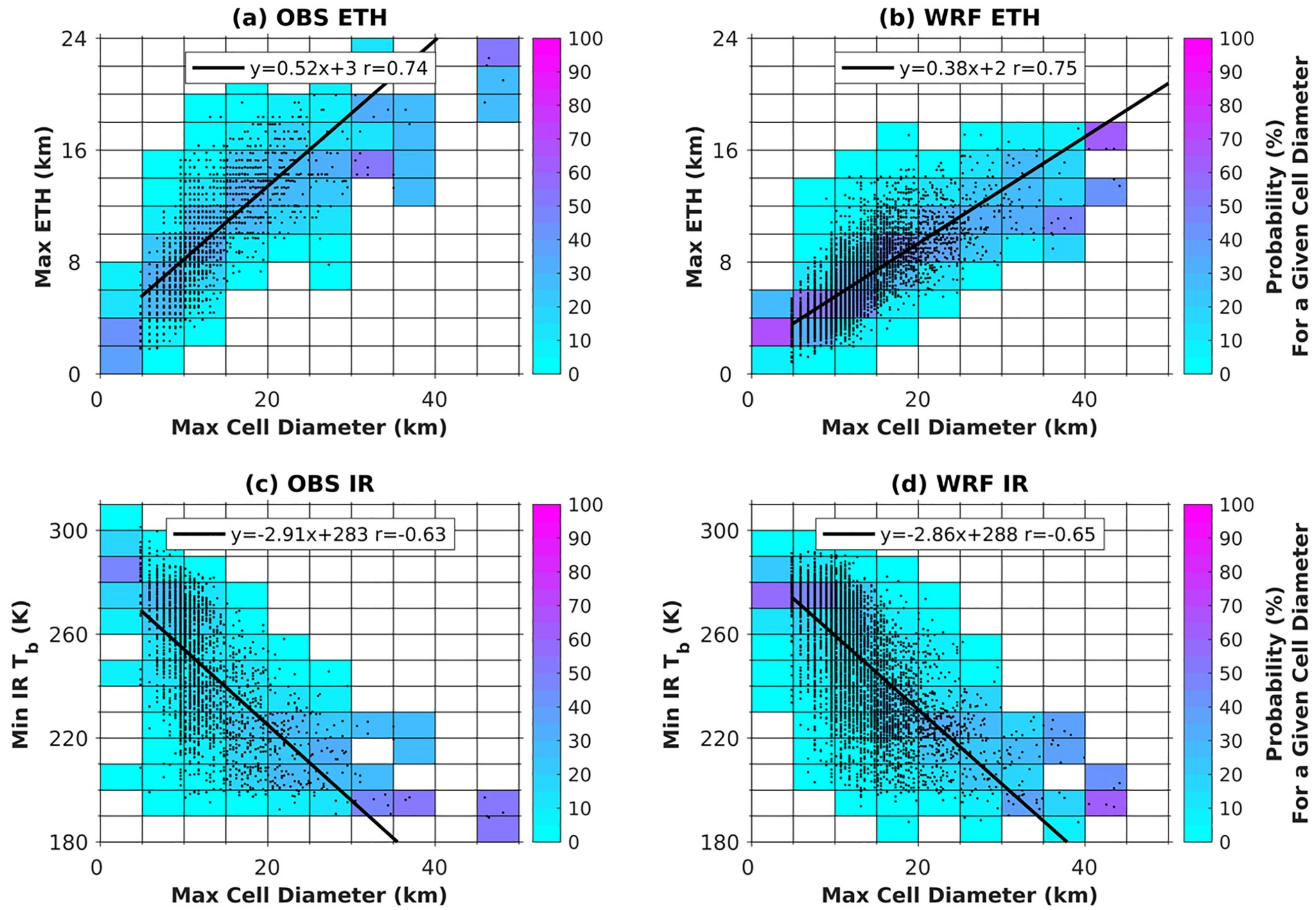

Figure 11. Observed and simulated (a–b) lifecycle-maximum 10-dBZ radar reflectivity ETH and (c–d) lifecycle-minimum TOA IR T_b as functions of lifecycle-maximum convective cell diameter. The color fill shows ETH and TOA IR T_b values conditions on maximum cell diameter. The ordinary least square fit lines are shown in black, and the *r* value represents the Pearson linear correlation coefficient.

that is typically twice the updraft area (174 km^2). This is substantially wider than most convective updrafts measured by aircraft (e.g., Anderson et al., 2005; Lucas et al., 1994; Warner & McNamara, 1984) and radar wind profilers (e.g., Wang et al., 2020). Indeed, more than 2/3 of convective cell areas defined on a 500-m spaced grid are smaller than the minimum resolvable areal threshold (174 km^2) at 3-km grid spacing (Figure S7 in Supporting Information S1). This could result in a shift of energy from unresolvable small cells into larger resolvable cell sizes in the simulation, possibly contributing to the previously discussed model biases.

6. Bias Sensitivity to Model Resolution

To test how increased model resolution affects simulated convective cell and convective-stratiform partitioning biases, low and high CAPE events were chosen (Table 1) and simulated with nested 1- and 0.333-km horizontal grid spacing domains to compare with the 3-km grid spacing results (see Section 2.2 for details). Observations were also analyzed on a 500-m horizontal grid in addition to the 3-km grid. All results in this section apply to the individual low and high CAPE events, though 3-km results are generally consistent with the season-long simulation results.

In the low CAPE case (black dots in Figure 12), convective rain volumes are overestimated by more than 84% in all 3 simulations (Figure 12b). The simulated convective rain volumes in the 3-km and 1-km runs are similar, but the 0.333-km run produces about 25% more convective rainfall than coarser simulations (Figure 12a). Figures 12c and 12d shows that the 3-km run accurately predicts the stratiform rainfall, but the 1-km and 0.333-km runs underestimate it by 24% and 46%, respectively. In Figure 12e–f, 1-km and 0.333-km convective and stratiform biases offset to produce total rainfall that is similar to observed in the low CAPE case while the 3-km run

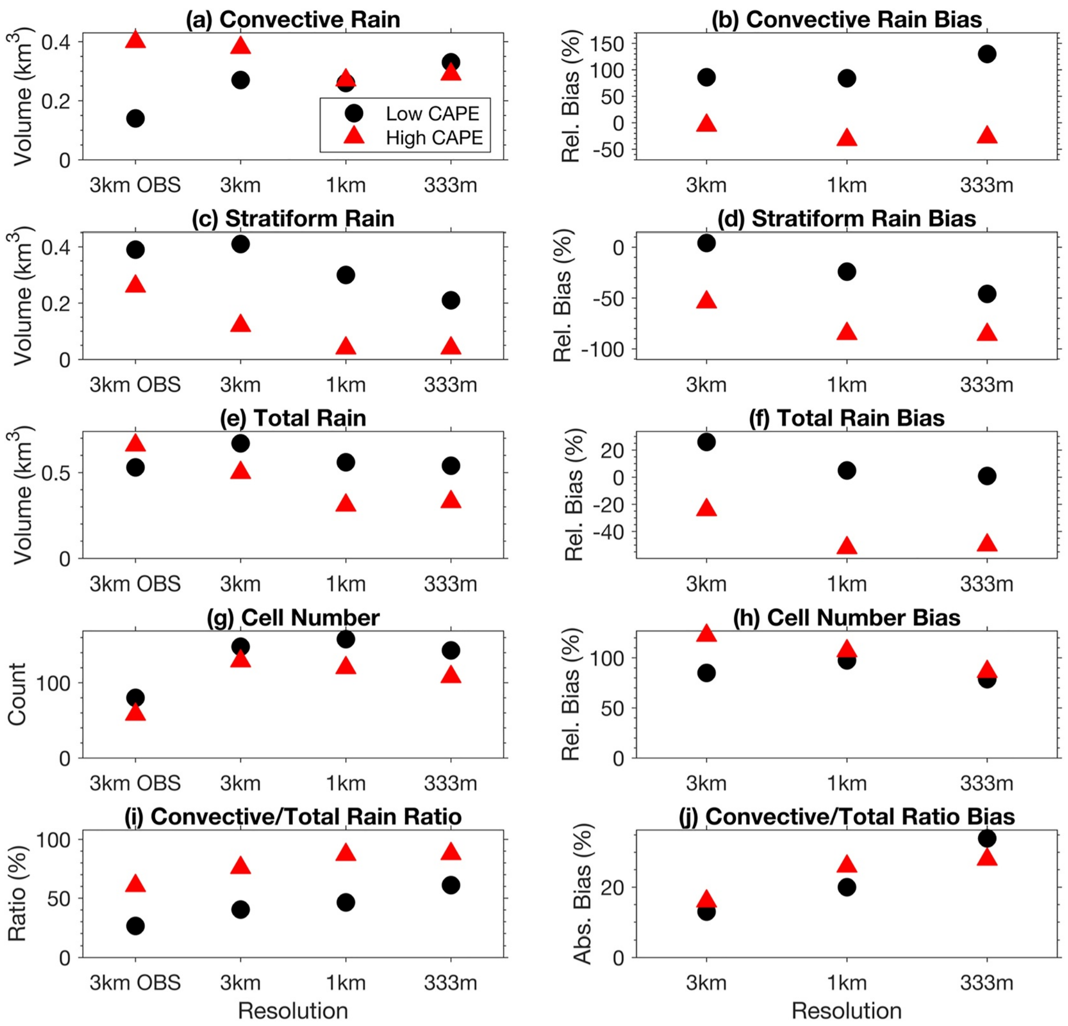

Figure 12. Rainfall differences in 3-, 1-, and 0.333-km horizontal grid spacing simulations and 3-km horizontal grid spacing observations for the low and high CAPE events.

overestimates rainfall by 26%. In Figures 12g and 12h, simulated cell numbers are nearly double those observed for all resolutions with the 1-km experiment producing the most numerous convective cells.

In contrast to the low CAPE case, the high CAPE case's convective rainfall is simulated accurately in the 3-km run but underestimated by ~30% in the 1-km and 0.333-km simulations (Figures 12a and 12b). Stratiform rainfall is greatly underestimated by the simulations, a bias that increases from −54% to −86% as horizontal grid spacing decreases from 3 to 0.333 km and is much worse than the low CAPE stratiform rainfall bias. The stratiform underproduction leads to total rainfall being underestimated by all simulations with 1-km and 0.333-km runs producing only half of what was observed due to additional contributions from underpredicted convective rainfall (Figures 12c and 12d). Simulated convective cell numbers are about double those observed for all model resolutions, similar to the low CAPE case (Figures 12g and 12h).

The convective contribution to total rainfall (Figures 12i and 12j) is also biased high for all simulations and increases as resolution increases for both low and high CAPE cases. Overall, stratiform rainfall biases and their biased contribution to total rainfall worsen as the model grid spacing decreases in these convective cases. This suggests that effectively reducing the stratiform bias cannot be achieved solely via increasing the model's resolution, pointing to physics parameterization contributions that require further evaluation. Additionally, some biases do not monotonically change with model resolution and vary between low and high CAPE cases, which agrees with some past studies (e.g., Bryan et al., 2003; Prein et al., 2021).

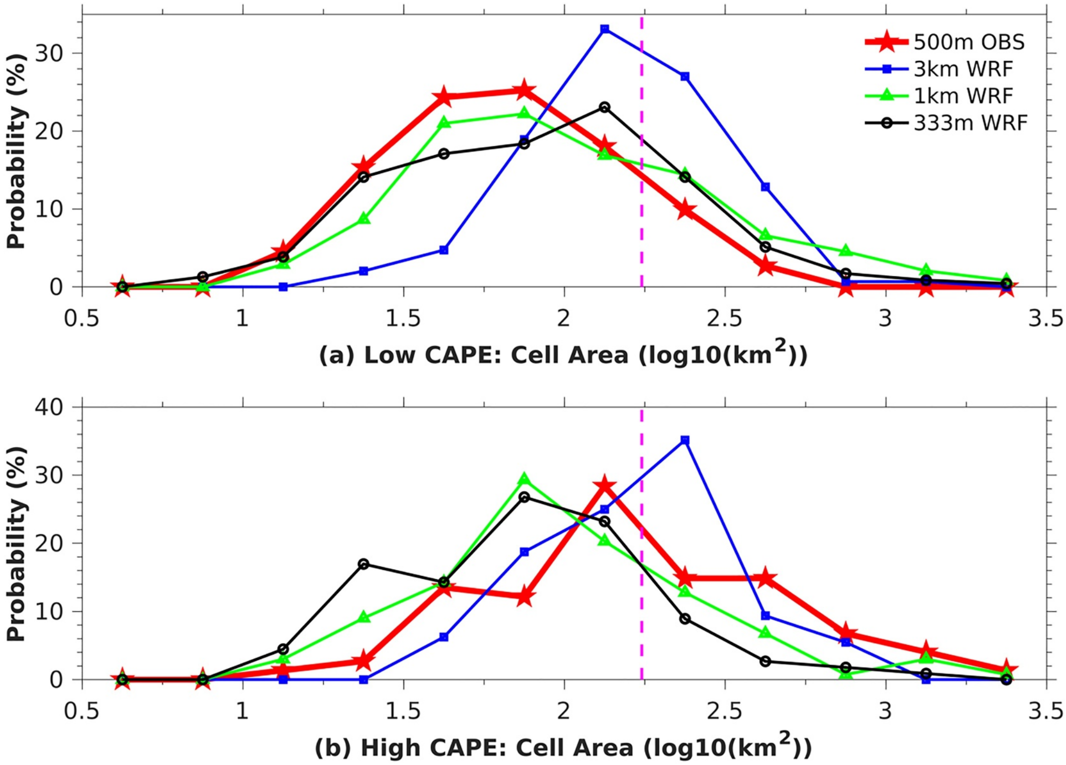

Figure 13. PDFs of convective cell areas for the (a) low and (b) high CAPE events for full resolution data sets (not averaged to 3-km grid spacing) except for the 0.333-km run that is averaged to 500 m to match 500-m observations. The vertical dashed lines represent the approximate minimum resolvable cell area in WRF with 3-km horizontal grid spacing.

Convective cell properties also vary substantially by resolution. In the low CAPE event, the 3-km run significantly underestimates the probability of convective cells at sizes smaller than 80 km^2 (Figure 13a; 1.9 on the log10 scale). The 1-km and 0.333-km runs produce more small cells than the 3-km run, aligning more closely with observations. The 1-km run matches the observed distribution best when log10(cell area) is between 1.5 and 2.5, while the 0.333-km run performs better for the tails of the distribution (log10(cell area) <1.5 and >2.5). This suggests that reducing model grid spacing below 500 m may better resolve convective cells and improve predictions for the tails of the cell area distribution. Kolmogorov-Smirnov (KS) testing of differences between observed and simulated cell area distributions further demonstrates that *p* values increase as model resolution increases from 5×10^{-13} to 0.007 and 0.05 for 3-, 1-, and 0.333-km runs, respectively. Thus, at a 5% level, 3-km and 1-km runs significantly differ from observations while the simulated area distribution in the 0.333-km run does not. In the high CAPE event, the observed convective cells are larger than those in the low CAPE case (Figure 13). More convective cells in the 3-km simulation are shifted to the right side of the dashed line and better resolved in these conditions as compared to the low CAPE event. The 3-km run also better agrees with the observed cell area distribution for this high CAPE event (p value = 0.1) than the 1-km and 0.333-km runs (p values of 0.001 and 0.0001, respectively). The simulated updraft width distribution differences (Figure S8 in Supporting Information S1) largely follow the cell area distribution differences in Figure 13, showing that updrafts become better resolved with increasing resolution with cell areas being a decent proxy for updraft area. However, all resolutions fail to reproduce the notable shift from small to large cell sizes that is observed with increasing CAPE (Figures 13a and 13b) without universal improvement of cell areas with resolution across both low and high CAPE conditions.

Despite shifts to smaller cell and updraft areas as model resolution increases, Figure S9 in Supporting Information S1 shows that convective cell depth is greatly underestimated across all resolutions in both low and high CAPE conditions. Thus, all simulations, regardless of resolution, produce more numerous shallow cells than observed that dominate the PDFs, with the caveat that a portion of the difference is also due to high biased ETHs in observations. In both low and high CAPE events, simulated shallow cell echo tops peak between 4 and 7 km

AMSL. The excessive number of these relatively shallow cells amplify convective rainfall with little contribution to stratiform rainfall growth. Collectively, the model resolution sensitivity tests suggest that insufficient model resolution is not the primary cause for convective cell area, depth, and stratiform growth biases. This suggests that physics parameterizations such as the microphysics scheme's control on precipitation formation and growth are potentially primary contributors to cell number, cell depth, and convective-stratiform partitioning biases.

7. Conclusions

This study evaluated the accuracy of convective cell and system growth in a season-long convection-permitting WRF simulation with 3-km horizontal grid spacing using RELAMPAGO-CACTI field campaign measurements. Observed and simulated cells were analogously defined and tracked with results assessed in the context of atmospheric instability as represented by CAPE, which was found to modulate model biases.

The simulation reproduced the observed total rainfall in low CAPE conditions and only slightly underestimated it in high CAPE conditions. However, when separating rainfall into convective and stratiform components, large biases were found, including:

- Convective rainfall was overestimated by 43% in the simulation, a bias that decreased with CAPE. However, simulated stratiform rainfall was underestimated by 46%, a bias that increased with CAPE.
- Stratiform rainfall increased with convective rainfall, but the simulation required about double the convective rainfall to produce a similar amount of stratiform rainfall as that observed.
- The large model overestimation of the convective contribution to total rainfall remained approximately constant at 26% through all CAPE conditions.

Convective and stratiform rainfall partitioning biases were related to the model representation of convective cell number, area, depth, and growth characteristics, producing the following results:

- The simulation contained 2.6 times the number of cells that were observed, primarily through the production of excessive numbers of relatively shallow cells (4–7-km cell tops). The model required a wider convective cell to reach the same convective depth as observed.
- The overproduction of simulated cells increases as CAPE decreases because these conditions result in more numerous shallow and narrow updrafts as compared to high CAPE conditions.
- Relatively large cells contributed the most to convective rainfall biases, with contributions increasing as CAPE decreased. Despite this, cell growth processes via expansion, shrinking, merging, and splitting show limited differences between observations and the simulation.

Possible controls of model resolution upon simulated convective cell biases were investigated in simulations of representative cases containing low and high CAPE conditions using 3-km, 1-km, and 0.333-km horizontal grid spacing. Simulated convective cell area was proportional to updraft area, indicating that radar reflectivity observations may be able to inform updraft width. A large proportion of convective cell areas defined using 500-m grid spacing radar observations were not fully resolvable with 3-km horizontal grid spacing in WRF, with small area cells that reached depths of less than 7 km being the worst resolved. Comparing analogous cell precipitation characteristics across model resolutions resulted in the following conclusions:

- The high cell number bias noted in the 3-km simulation was not mitigated by increasing model grid resolution.
- Despite better spatially resolving convective updrafts and cells, increasing model resolution amplified the simulated underestimation of stratiform rainfall and the overestimation of convective contribution to total rainfall.
- Total rainfall and cell areas during the low CAPE event were best captured by the 0.333-km run. However, these properties were best captured by the 3-km run during the high CAPE event.

This study implies that substantial convective cell and system rainfall biases can exist in continental convection-permitting simulations with settings commonly used in regional weather and climate modeling with strong modulation by environmental instability. Increasing model resolution by an order of magnitude neither reduces excessive numbers of precipitating congestus clouds nor decreases ratios of convective to stratiform precipitation, suggesting that improving prediction of deep convective system growth depends on factors beyond solely increasing model resolution. Following findings in past studies, a potentially substantial contributor to biases is the cloud microphysics parameterization that may promote too efficient precipitation formation and growth in congestus clouds with excessive supercooled liquid and riming in mixed phase clouds, which would strongly modulate convective cell identification and convective-stratiform precipitation partitioning.

Future work could build on this study in several ways. First, further research is needed to identify causes for the excessive production of relatively shallow convective cells and how this interacts with underproduced stratiform precipitation. Second, the sensitivity of results to the temporal resolution of reflectivity could be assessed since 15 min is too coarse to capture cells with short lifetimes and introduces uncertainty into cell start and end time as well as identification of splitting and merging events. Sensitivity to minimum cell overlap between times could also be assessed. Third, further work is needed to assess how these findings apply to other meteorological regimes and model setups, particularly in relation to sensitivity to different microphysics schemes. For example, prior research by Feng et al. (2018) showed that both the Thompson and Morrison schemes underestimated MCS stratiform rainfall over the continental U.S., though the Thompson scheme produced more stratiform rainfall. As highlighted in the introduction, several model intercomparison studies have also shown that MCS stratiform precipitation is insufficient across a variety of microphysics schemes. However, biases do vary by scheme, and it is unclear how the convective cell biases shown here vary as a function of model setup, highlighting the need for further studies.

Data Availability Statement

The model setup for WRF runs and the observed and simulated convective cell track data sets are available here: https://doi.org/10.5281/zenodo.10655168 (Zhang et al., 2024a). The configuration for PyFLEXTRKR in this study can be accessed via at https://doi.org/10.5281/zenodo.13760822 (Zhang et al., 2024b). The radar measurements, satellite retrievals, and raw model output are large data sets that can be accessed by contacting the authors.

Acknowledgments

The study was funded by NSF project 1661662 and the U.S. Department of Energy (DOE) Office of Science Biological and Environmental Research as part of the Atmospheric System Research program. Pacific Northwest National Laboratory is operated by Battelle for the U.S. Department of Energy under Contract DE-AC05-76RLO1830. Computing and disk storage resources were provided by the NCAR Computational and Information Systems Laboratory and the University of Utah Center for High Performance Computing. Some data analysis was also performed using computational resources provided by the National Energy Research Scientific Computing Center, a DOE Office of Science User Facility supported under contract DE-AC02-05CH11231. We thank K. Ryder Fox (University of Miami) for contributing to the LES setup.

References

Anderson, N. F., Grainger, C. A., & Stith, J. L. (2005). Characteristics of strong updrafts in precipitation systems over the central Tropical Pacific Ocean and in the Amazon. *Journal of Applied Meteorology*, *44*(5), 731–738. https://doi.org/10.1175/JAM2231.1

Bretherton, C. S., & Park, S. (2009). A new moist turbulence parameterization in the community atmosphere model. *Journal of Climate*, *22*(12), 3422–3448. https://doi.org/10.1175/2008JCLI2556.1

Bryan, G. H., & Morrison, H. (2012). Sensitivity of a simulated squall line to horizontal resolution and parameterization of microphysics. *Monthly Weather Review*, *140*(1), 202–225. https://doi.org/10.1175/MWR-D-11-00046.1

Bryan, G. H., Wyngaard, J. C., & Fritsch, J. M. (2003). Resolution requirements for the simulation of deep moist convection. *Monthly Weather Review*, *131*(10), 2394–2416. https://doi.org/10.1175/1520-0493(2003)131<2394:RRFTSO>2.0.CO;2

Caine, S., Lane, T. P., May, P. T., Jakob, C., Siems, S. T., Manton, M. J., & Pinto, J. (2013). Statistical assessment of tropical convection-permitting model simulations using a cell-tracking algorithm. *Monthly Weather Review*, *141*(2), 557–581. https://doi.org/10.1175/MWR-D-11-00274.1

Casaretto, G., Dillon, M. E., Salio, P., Skabar, Y. G., Nesbitt, S. W., Schumacher, R. S., et al. (2021). High-resolution NWP forecast precipitation comparison over complex terrain of the Sierras de Córdoba during RELAMPAGO-CACTI. *Weather and Forecasting*, *37*(2), 241–266. https://doi.org/10.1175/WAF-D-21-0006.1

Chen, S. S., & Frank, W. M. (1993). A numerical study of the genesis of extratropical convective mesovortices. Part I: Evolution and dynamics. *Journal of the Atmospheric Sciences*, *50*(15), 2401–2426. https://doi.org/10.1175/1520-0469(1993)050<2401:ANSOTG>2.0.CO;2

Cifelli, R., Chandrasekar, V., Lim, S., Kennedy, P. C., Wang, Y., & Rutledge, S. A. (2011). A new dual-polarization radar rainfall algorithm: Application in Colorado precipitation events. *Journal of Atmospheric and Oceanic Technology*, *28*(3), 352–364. https://doi.org/10.1175/2010JTECHA1488.1

Clark, A. J., Bullock, R. G., Jensen, T. L., Xue, M., & Kong, F. (2014). Application of object-based time-domain diagnostics for tracking precipitation systems in convection-allowing models. *Weather and Forecasting*, *29*(3), 517–542. https://doi.org/10.1175/WAF-D-13-0098.1

Copernicus Climate Change Service. (2017). *ERA5: Fifth generation of ECMWF atmospheric reanalyses of the global climate. ECMWF, Reading, United Kingdom, Copernicus Climate Change Serv*. Climate Data Store (CDS). Retrieved from https://cds.climate.copernicus.eu/cdsapp#!/home. accessed 23 May 2019.

Craig, G. C., & Dörnbrack, A. (2008). Entrainment in cumulus clouds: What resolution is cloud-resolving? *Journal of the Atmospheric Sciences*, *65*(12), 3978–3988. https://doi.org/10.1175/2008JAS2613.1

Donner, L. J. (1993). A cumulus parameterization including mass fluxes, vertical momentum dynamics, and mesoscale effects. *Journal of the Atmospheric Sciences*, *50*(6), 889–906. https://doi.org/10.1175/1520-0469(1993)050<0889:ACPIMF>2.0.CO;2

Donner, L. J., Seman, C. J., Hemler, R. S., & Fan, S. (2001). A cumulus parameterization including mass fluxes, convective vertical velocities, and mesoscale effects: Thermodynamic and hydrological aspects in a general circulation model. *Journal of Climate*, *14*(16), 3444–3463. https://doi.org/10.1175/1520-0442(2001)014<3444:ACPIMF>2.0.CO;2

Dowell, D. C., Alexander, C. R., James, E. P., Weygandt, S. S., Benjamin, S. G., Manikin, G. S., et al. (2022). The high-resolution rapid refresh (HRRR): An hourly updating convection-allowing forecast model. Part I: Motivation and system description. *Weather and Forecasting*, *37*(8), 1371–1395. https://doi.org/10.1175/WAF-D-21-0151.1

Duda, J. D., & Turner, D. D. (2021). Large-sample application of radar reflectivity object-based verification to evaluate HRRR warm-season forecasts. *Weather and Forecasting*, *36*(3), 805–821. https://doi.org/10.1175/WAF-D-20-0203.1

Duda, J. D., & Turner, D. D. (2023). Using object-based verification to assess improvements in forecasts of convective storms between operational HRRR versions 3 and 4. *Weather and Forecasting*, *38*(10), 1971–1994. https://doi.org/10.1175/WAF-D-22-0181.1

Fairless, T., & Giangrande, S. (2018). *Interpolated sonde (INTERPOLATEDSONDE)*. ARM User Facility. https://doi.org/10.5439/1095316. accessed 8 March 2021.

Fan, J., Han, B., Varble, A., Morrison, H., North, K., Kollias, P., et al. (2017). Cloud-resolving model intercomparison of an MC3E squall line case: Part I – Convective updrafts. *Journal of Geophysical Research: Atmospheres*, *122*(17), 9351–9378. https://doi.org/10.1002/2017JD026622

Feng, Z., Hardin, J., Barnes, H. C., Li, J., Leung, L. R., Varble, A., & Zhang, Z. (2023). PyFLEXTRKR: A flexible feature tracking Python software for convective cloud analysis. *Geoscientific Model Development*, *16*(10), 2753–2776. https://doi.org/10.5194/gmd-16-2753-2023

Feng, Z., Leung, L. R., Hardin, J., Terai, C. R., Song, F., & Caldwell, P. (2023b). Mesoscale convective systems in DYAMOND global convection-permitting simulations. *Geophysical Research Letters*, *50*(4), e2022GL102603. https://doi.org/10.1029/2022GL102603

Feng, Z., Leung, L. R., Houze, R. A., Hagos, S., Hardin, J., Yang, Q., et al. (2018). Structure and evolution of mesoscale convective systems: Sensitivity to cloud microphysics in convection-permitting simulations over the United States. *Journal of Advances in Modeling Earth Systems*, *10*(7), 1470–1494. https://doi.org/10.1029/2018MS001305

Feng, Z., Varble, A., Hardin, J., Marquis, J., Hunzinger, A., Zhang, Z., & Thieman, M. (2022). Deep convection initiation, growth, and environments in the complex terrain of central Argentina during CACTI. *Monthly Weather Review*, *150*(5), 1135–1155. https://doi.org/10.1175/mwr-d-21-0237.1

Gamache, J., & Houze, R. A. (1983). Water budget of a mesoscale convective system in the tropics. *Journal of the Atmospheric Sciences*, *40*(7), 1835–1850. https://doi.org/10.1175/1520-0469(1983)040<1835:WBOAMC>2.0.CO;2

Giangrande, S. E., Collis, S., Theisen, A. K., & Tokay, A. (2014). Precipitation estimation from the ARM distributed radar network during the MC3E campaign. *Journal of Applied Meteorology and Climatology*, *53*(9), 2130–2147. https://doi.org/10.1175/JAMC-D-13-0321.1

Giangrande, S. E., McGraw, R., & Lei, L. (2013). An application of linear programming to polarimetric radar differential phase processing. *Journal of Atmospheric and Oceanic Technology*, *30*(8), 1716–1729. https://doi.org/10.1175/JTECH-D-12-00147.1

Glenn, I. B., & Krueger, S. K. (2017). Connections matter: Updraft merging in organized tropical deep convection. *Geophysical Research Letters*, *44*(13), 7087–7094. https://doi.org/10.1002/2017GL074162

Grim, J. A., Pinto, J. O., Blitz, T., Stone, K., & Dowell, D. C. (2021). Biases in the prediction of convective storm characteristics with a convection allowing ensemble. *Weather and Forecasting*, *37*(1), 65–83. https://doi.org/10.1175/WAF-D-21-0106.1

Hagos, S., Feng, Z., Burleyson, C. D., Lim, K. S. S., Long, C. N., Wu, D., & Thompson, G. (2014). Evaluation of convection-permitting model simulations of cloud populations associated with the Madden-Julian oscillation using data collected during the AMIE/DYNAMO field campaign. *Journal of Geophysical Research*, *119*(21), 12052–12068. https://doi.org/10.1002/2014JD022143

Han, B., Fan, J., Varble, A., Morrison, H., Williams, C. R., Chen, B., et al. (2019). Cloud-resolving model intercomparison of an MC3E squall line case: Part II. Stratiform precipitation properties. *Journal of Geophysical Research: Atmospheres*, *124*(2), 1090–1117. https://doi.org/10.1029/2018JD029596

Hardin, J., Bharadwaj, N., Giangrande, S. E., Varble, A., & Feng, Z. (2020). Taranis: A new framework for physically constrained radar processing. In *2020 fall meeting, online, American Geophysical Union, Abstract A159-08*. Retrieved from https://agu.confex.com/agu/fm20/meetingapp.cgi/Paper/699052

Hardin, J., Bharadwaj, N., Varble, A., Giangrande, S., & Feng, Z. (2024). *PI Data: CACTI CSAPR2 Taranis Retrievals*. https://doi.org/10.5439/2440152

Hardin, J., Giangrande, S. E., & Zhou, A. (2020). *Laser disdrometer quantities (LDQUANTS) and video disdrometer quantities (VDISQUANTS) value-added products report* (p. 12). ARM Technical Document DOE/SC-ARM-TR-221.

Hardin, J., Hunzinger, A., Schuman, E., Matthews, A., Bharadwaj, N., Varble, A., et al. (2018). *C-band scanning ARM precipitation radar, CF-radial, quality-controlled plan position indicator scans (CSAPR2CFRPPIQC)*. ARM User Facility. https://doi.org/10.5439/1615604. accessed 9 March 2021.

Hardin, J., Hunzinger, A., Schuman, E., Matthews, A., Bharadwaj, N., Varble, A., et al. (2020). *CACTI radar b1 processing: Corrections, calibrations, and processing report* (p. 46). ARM Technical Document DOE/SC-ARM-TR-244.

Heistermann, M., Jacobi, S., & Pfaff, T. (2013). Technical note: An open source library for processing weather radar data (wradlib). *Hydrology and Earth System Sciences*, *17*(2), 863–871. https://doi.org/10.5194/hess-17-863-2013

Helmus, J. J., & Collis, S. M. (2016). The Python ARM radar toolkit (Py-ART), a library for working with weather radar data in the python programming language. *Journal of Open Research Software*, *4*(1), e25. https://doi.org/10.5334/jors.119

Houze, R. A. (2004). Mesoscale convective systems. *Reviews of Geophysics*, *42*(4), RG4003. https://doi.org/10.1029/2004RG000150

Iacono, M. J., Delamere, J. S., Mlawer, E. J., Shephard, M. W., Clough, S. A., & Collins, W. D. (2008). Radiative forcing by long-lived greenhouse gases: Calculations with the AER radiative transfer models. *Journal of Geophysical Research*, *113*(D13), D13103. https://doi.org/10.1029/2008JD009944

Janjic, Z. (2002). *Nonsingular implementation of the Mellor-Yamada level 2.5 scheme in the NCEP Meso model* (Vol. 437, p. 61). National Center for Environmental Prediction Office Note.

Jeevanjee, N., & Zhou, L. (2022). On the resolution-dependence of anvil cloud fraction and precipitation efficiency in radiative-convective equilibrium. *Journal of Advances in Modeling Earth Systems*, *14*(3), e2021MS002759. https://doi.org/10.1029/2021MS002759

Kyrouac, J., Shi, Y., Jane, M., & Wang, D. (2018). *Rain gauge (RAINTB)*. ARM User Facility. https://doi.org/10.5439/1224827. accessed 30 August 2024.

Lakshmanan, V., Hondl, K., Potvin, C. K., & Preignitz, D. (2013). An improved method for estimating radar echo-top height. *Weather and Forecasting*, *28*(2), 481–488. https://doi.org/10.1175/WAF-D-12-00084.1

Lareau, N. P., Knopp, T., & Kirshbaum, D. J. (2024). Mechanical and thermal forcing for upslope flows and cumulus convection over the Sierras de Cordoba. *Monthly Weather Review*, *152*(9), 2149–2167. https://doi.org/10.1175/MWR-D-23-0254.1

Lebo, Z. J., & Morrison, H. (2015). Effects of horizontal and vertical grid spacing on mixing in simulated squall lines and implications for convective strength and structure. *Monthly Weather Review*, *143*(11), 4355–4375. https://doi.org/10.1175/MWR-D-15-0154.1

Lim, S., & Chandrasekar, V. (2016). A robust attenuation correction system for reflectivity and differential reflectivity in weather radars. *IEEE Transactions on Geoscience and Remote Sensing*, *54*(3), 1727–1737. https://doi.org/10.1109/TGRS.2015.2487984

Liu, C., Shige, S., Takayabu, Y. N., & Zipser, E. (2015). Latent heating contribution from precipitation systems with different sizes, depths, and intensities in the tropics. *Journal of Climate*, *28*(1), 186–203. https://doi.org/10.1175/JCLI-D-14-00370.1

Lucas, C., Zipser, E. J., & LeMone, M. A. (1994). Vertical velocity in oceanic convection off tropical Australia. *Journal of the Atmospheric Sciences*, *51*(21), 3183–3193. https://doi.org/10.1175/1520-0469(1994)051<3183:VVIOCO>2.0.CO;2

Marquis, J. N., Feng, Z., Varble, A., Nelson, T. C., Houston, A., Peters, J. M., et al. (2023). Near-cloud atmospheric ingredients for deep convection initiation. *Monthly Weather Review*, *151*(5), 1247–1267. https://doi.org/10.1175/MWR-D-22-0243.1

Marquis, J. N., Varble, A. C., Robinson, P., Nelson, T. C., & Friedrich, K. (2021). Low-level mesoscale and cloud-scale interactions promoting deep convection initiation. *Monthly Weather Review*, *149*(8), 2473–2495. https://doi.org/10.1175/MWR-D-20-0391.1

Morrison, H. (2016). Impacts of updraft size and dimensionality on the perturbation pressure and vertical velocity in cumulus convection. Part II: Comparison of theoretical and numerical solutions and fully dynamical simulations. *Journal of the Atmospheric Sciences*, *73*(4), 1455–1480. https://doi.org/10.1175/JAS-D-15-0041.1

Morrison, H., Morales, A., & Villanueva-Birriel, C. (2015). Concurrent sensitivities of an idealized deep convective storm to parameterization of microphysics, horizontal grid resolution, and environmental static stability. *Monthly Weather Review*, *143*(6), 2082–2104. https://doi.org/10.1175/MWR-D-14-00271.1

Mulholland, J. P., Nesbitt, S. W., & Trapp, R. J. (2019). A case study of terrain influences on upscale convective growth of a supercell. *Monthly Weather Review*, *147*(12), 4305–4324. https://doi.org/10.1175/MWR-D-19-0099.1

Mulholland, J. P., Nesbitt, S. W., Trapp, R. J., Rasmussen, K. L., & Salio, P. V. (2018). Convective storm life cycle and environments near the Sierras de Córdoba, Argentina. *Monthly Weather Review*, *146*(8), 2541–2557. https://doi.org/10.1175/MWR-D-18-0081.1

Nakanishi, M., & Niino, H. (2006). An improved Mellor-Yamada Level-3 model: Its numerical stability and application to a regional prediction of advection fog. *Boundary-Layer Meteorology*, *119*(2), 397–407. https://doi.org/10.1007/s10546-005-9030-8

Nakanishi, M., & Niino, H. (2009). Development of an improved turbulence closure model for the atmospheric boundary layer. *Journal of the Meteorological Society of Japan*, *87*(5), 895–912. https://doi.org/10.2151/jmsj.87.895

Nelson, T. C., Marquis, J., Peters, J. M., & Friedrich, K. (2022). Environmental controls on simulated deep moist convection initiation occurring during RELAMPAGO-CACTI. *Journal of the Atmospheric Sciences*, *79*(6), 1941–1964. https://doi.org/10.1175/JAS-D-21-0226.1

Nelson, T. C., Marquis, J., Varble, A., & Friedrich, K. (2021). Radiosonde observations of environments supporting deep moist convection initiation during RELAMPAGO-CACTI. *Monthly Weather Review*, *149*(1), 289–309. https://doi.org/10.1175/MWR-D-20-0148.1

Nesbitt, S. W., Salio, P. V., Ávila, E., Bitzer, P., Carey, L., Chandrasekar, V., et al. (2021). A Storm Safari in Subtropical South America: Proyecto RELAMPAGO. *Bulletin of the American Meteorological Society*, *102*(8), E1621–E1644. https://doi.org/10.1175/BAMS-D-20-0029.1

Nicol, J. C., Hogan, R. J., Stein, T. H. M., Hanley, K. E., Clark, P. A., Halliwell, C. E., et al. (2015). Convective updraught evaluation in high resolution NWP simulations using single-Doppler radar measurements. *Quarterly Journal of the Royal Meteorological Society*, *141*(693), 3177–3189. https://doi.org/10.1002/qj.2602

Pan, D.-M., & Randall, D. D. A. (1998). A cumulus parameterization with a prognostic closure. *Quarterly Journal of the Royal Meteorological Society*, *124*(547), 949–981. https://doi.org/10.1002/qj.49712454714

Petch, J. C., Brown, A. R., & Gray, M. E. B. (2002). The impact of horizontal resolution on the simulations of convective development over land. *Quarterly Journal of the Royal Meteorological Society*, *128*(584), 2031–2044. https://doi.org/10.1256/003590002320603511

Piersante, J. O., Rasmussen, K. L., Schumacher, R. S., Rowe, A. K., & McMurdie, L. A. (2021). A Synoptic evolution comparison of the smallest and largest MCSS in subtropical South America between spring and summer. *Monthly Weather Review*, *149*(6), 1943–1966. https://doi.org/10.1175/MWR-D-20-0208.1

Prein, A. F., Gobiet, A., Suklitsch, M., Truhetz, H., Awan, N. K., Keuler, K., & Georgievski, G. (2013). Added value of convection permitting seasonal simulations. *Climate Dynamics*, *41*(9–10), 2655–2677. https://doi.org/10.1007/s00382-013-1744-6

Prein, A. F., Liu, C., Ikeda, K., Bullock, R., Rasmussen, R. M., Holland, G. J., & Clark, M. (2017). Simulating North American mesoscale convective systems with a convection-permitting climate model. *Climate Dynamics*, *55*(1–2), 95–110. https://doi.org/10.1007/s00382-017-3993-2

Prein, A. F., Rasmussen, R. M., Wang, D., & Giangrande, S. (2021). Sensitivity of organized convective storms to model grid spacing in current and future climates. *Philosophical Transactions of the Royal Society A*, *379*(2195), 20190546. https://doi.org/10.1098/rsta.2019.0546

Rasmussen, K. L., & Houze, R. A. (2011). Orogenic convection in subtropical South America as seen by the TRMM satellite. *Monthly Weather Review*, *139*(8), 2399–2420. https://doi.org/10.1175/MWR-D-10-05006.1

Rasmussen, K. L., & Houze, R. A. (2016). Convective initiation near the Andes in subtropical South America. *Monthly Weather Review*, *144*(6), 2351–2374. https://doi.org/10.1175/MWR-D-15-0058.1

Ribeiro, B. Z., & Bosart, L. F. (2018). Elevated mixed layers and associated severe thunderstorm environments in South and North America. *Monthly Weather Review*, *146*(1), 3–28. https://doi.org/10.1175/MWR-D-17-0121.1

Rocque, M. N., & Rasmussen, K. L. (2022). The impact of topography on the environment and life cycle of weakly and strongly forced MCSs during RELAMPAGO. *Monthly Weather Review*, *150*(9), 2317–2338. https://doi.org/10.1175/MWR-D-22-0049.1

Rotunno, R., Klemp, J. B., & Weisman, M. L. (1988). A theory for strong, long-lived squall lines. *Journal of the Atmospheric Sciences*, *45*(3), 463–485. https://doi.org/10.1175/1520-0469(1988)045<0463:ATFSLL>2.0.CO;2

Ryzhkov, A. V., Giangrande, S. E., & Schuur, T. J. (2005). Rainfall estimation with a polarimetric prototype of WSR-88D. *Journal of Applied Meteorology and Climatology*, *44*(4), 502–515. https://doi.org/10.1175/JAM2213.1

Salio, P., Nicolini, M., & Saulo, A. C. (2002). Chaco low-level jet events characterization during the austral summer season. *Journal of Geophysical Research*, *107*(D24), 4816. https://doi.org/10.1029/2001JD001315

Salio, P., Nicolini, M., & Zipser, E. J. (2007). Mesoscale convective systems over southeastern South America and their relationship with the South American low-level jet. *Monthly Weather Review*, *135*(4), 1290–1309. https://doi.org/10.1175/MWR3305.1

Sasaki, C. R. S., Rowe, A. K., McMurdie, L. A., & Rasmussen, K. L. (2022). New insights into the South American low-level jet from RELAMPAGO observations. *Monthly Weather Review*, *150*(6), 1247–1271. https://doi.org/10.1175/MWR-D-21-0161.1

Sasaki, C. R. S., Rowe, A. K., McMurdie, L. A., Varble, A. C., & Zhang, Z. (2024). Influences of the South American low-level jet on the convective environment in Central Argentina using a convection-permitting simulation. *Monthly Weather Review*, *152*(2), 629–648. https://doi.org/10.1175/MWR-D-23-0122.1

Schumacher, C., Houze, R. A., & Kraucunas, I. (2004). The tropical dynamical response to latent heating estimates derived from the TRMM precipitation radar. *Journal of the Atmospheric Sciences*, *61*(12), 1341–1358. https://doi.org/10.1175/1520-0469(2004)061<1341:TTDRTL>2.0.CO;2

Schumacher, R. S., Hence, D. A., Nesbitt, S. W., Trapp, R. J., Kosiba, K. A., Wurman, J., et al. (2021). Convective-storm environments in subtropical South America from high-frequency soundings during Relampago-Cacti. *Monthly Weather Review*, *149*(5), 1439–1458. https://doi.org/10.1175/MWR-D-20-0293.1

Seluchi, M. E., Saulo, A. C., Nicolini, M., & Satyamurty, P. (2003). The Northwestern Argentinean Low: A study of two typical events. *Monthly Weather Review*, *131*(10), 2361–2378. https://doi.org/10.1175/1520-0493(2003)131<2361:TNALAS>2.0.CO;2

Singh, I., Nesbitt, S. W., & Davis, C. A. (2022). Quasi-idealized numerical simulations of processes involved in orogenic convection initiation over the Sierras de Córdoba. *Journal of the Atmospheric Sciences*, *79*(4), 1127–1149. https://doi.org/10.1175/JAS-D-21-0007.1

Skamarock, W. C. (2004). Evaluating mesoscale NWP models using kinetic energy spectra. *Monthly Weather Review*, *132*(12), 3019–3032. https://doi.org/10.1175/MWR2830.1

Skamarock, W. C., Klemp, J. B., Dudhia, J., Gill, D. O., Liu, Z., Berner, J., et al. (2019). *A description of the advanced research WRF model version 4*. NCAR Technical Note NCAR/TN-556+STR.

Smith, W. L., & Thieman, M. (2019). *Minnis cloud products using VISST algorithm (VISSTPX2DRECTG16V4MINNIS)*. ARM User Facility. Retrieved from https://adc.arm.gov/discovery/#/results/s::corvisstpx2drectg16v4minnisX1.c1

Stanford, M. W., Morrison, H., & Varble, A. (2020). Impacts of stochastic mixing in idealized convection-permitting simulations of squall lines. *Monthly Weather Review*, *148*(12), 4971–4994. https://doi.org/10.1175/mwr-d-20-0135.1

Stanford, M. W., Varble, A., Zipser, E., Strapp, J. W., Leroy, D., Schwarzenboeck, A., et al. (2017). A ubiquitous ice size bias in simulations of tropical deep convection. *Atmospheric Chemistry and Physics*, *17*(15), 9599–9621. https://doi.org/10.5194/acp-17-9599-2017

Stanford, M. W., Varble, A. C., & Morrison, H. (2024). Evaluation of a stochastic mixing scheme in the deep convective gray zone using a tropical oceanic deep convection case study. *Journal of Advances in Modeling Earth Systems*, *16*(1), e2023MS003748. https://doi.org/10.1029/2023MS003748

Stein, T. H. M., Hogan, R. J., Clark, P. A., Halliwell, C. E., Hanley, K. E., Lean, H. W., et al. (2015). The DYMECS project: A statistical approach for the evaluation of convective storms in high-resolution NWP models. *Bulletin of the American Meteorological Society*, *96*(6), 939–951. https://doi.org/10.1175/BAMS-D-13-00279.1

Steiner, M., Houze, R. A., & Yuter, S. E. (1995). Climatological characterization of three-dimensional storm structure from operational radar and rain gauge data. *Journal of Applied Meteorology*, *34*(9), 1978–2007. https://doi.org/10.1175/1520-0450(1995)034<1978:CCOTDS>2.0.CO;2

Thompson, G., & Eidhammer, T. (2014). A study of aerosol impacts on clouds and precipitation development in a large winter cyclone. *Journal of the Atmospheric Sciences*, *71*(10), 3636–3658. https://doi.org/10.1175/JAS-D-13-0305.1

Trapp, R. J., Kosiba, K. A., Marquis, J. N., Kumjian, M. R., Nesbitt, S. W., Wurman, J., et al. (2020). Multiple-platform and multiple-Doppler radar observations of a supercell thunderstorm in South America during Relampago. *Monthly Weather Review*, *148*(8), 3225–3241. https://doi.org/10.1175/MWR-D-20-0125.1

Varble, A., Fridlind, A. M., Zipser, E. J., Ackerman, A. S., Chaboureau, J. P., Fan, J., et al. (2011). Evaluation of cloud-resolving model intercomparison simulations using TWP-ICE observations: Precipitation and cloud structure. *Journal of Geophysical Research*, *116*(D12), D12206. https://doi.org/10.1029/2010JD015180

Varble, A. C., Feng, Z., Marquis, J. N., Zhang, Z., Geiss, A., Hardin, J. C., & Jo, E. (2024). *Updraft width modulates ambient atmospheric controls on deep convection depth*. ESS Open Archive. https://doi.org/10.22541/essoar.172656696.65404062/v1

Varble, A. C., Morrison, H., & Zipser, E. (2020). Effects of under-resolved convective dynamics on the evolution of a squall line. *Monthly Weather Review*, *148*(1), 289–311. https://doi.org/10.1175/mwr-d-19-0187.1

Varble, A. C., Nesbitt, S. W., Salio, P., Hardin, J. C., Bharadwaj, N., Borque, P., et al. (2021). Utilizing a storm-generating hotspot to study convective cloud transitions: The CACTI experiment. *Bulletin of the American Meteorological Society*, *102*(8), E1597–E1620. https://doi.org/10.1175/BAMS-D-20-0030.1

Varble, A. C., Zipser, E. J., Fridlind, A. M., Zhu, P., Ackerman, A. S., Chaboureau, J. P., et al. (2014a). Evaluation of cloud-resolving and limited area model intercomparison simulations using TWP-ICE observations: 1. Deep convective updraft properties. *Journal of Geophysical Research*, *119*(24), 13891–13918. https://doi.org/10.1002/2013JD021371

Varble, A. C., Zipser, E. J., Fridlind, A. M., Zhu, P., Ackerman, A. S., Chaboureau, J.-P., et al. (2014b). Evaluation of cloud-resolving and limited area model intercomparison simulations using TWP-ICE observations: 1. Precipitation microphysics. *Journal of Geophysical Research: Atmospheres*, *119*(24), 13919–13945. https://doi.org/10.1002/2013JD021372

Varble, A., Thieman, M., Spangenberg, D., Bedka, K., Smith, W., & Hardin, J. (2024). *PI Data: Parallax-corrected VISST-derived pixel-level products from satellite GOES-16*. https://doi.org/10.5439/2008448

Vera, C., Baez, J., Douglas, M., Emmanuel, C. B., Marengo, J., Meitin, J., et al. (2006). The South American low-level jet experiment. *Bulletin of the American Meteorological Society*, *87*(1), 63–78. https://doi.org/10.1175/BAMS-87-1-63

Wang, D., Giangrande, S. E., Feng, Z., Hardin, J. C., & Prein, A. F. (2020). Updraft and downdraft core size and intensity as revealed by radar wind profilers: MCS observations and idealized model comparisons. *Journal of Geophysical Research: Atmospheres*, *125*(11), e2019JD031774. https://doi.org/10.1029/2019JD031774

Wang, D., Prein, A. F., Giangrande, S. E., Ramos-Valle, A., Ge, M., & Jensen, M. P. (2022). Convective updraft and downdraft characteristics of continental mesoscale convective systems in the model gray zone. *Journal of Geophysical Research: Atmospheres*, *127*(16), e2022JD036746. https://doi.org/10.1029/2022JD036746

Wang, Y., & Chandrasekar, V. (2009). Algorithm for estimation of the specific differential phase. *Journal of Atmospheric and Oceanic Technology*, *26*(12), 2565–2578. https://doi.org/10.1175/2009JTECHA1358.1

Warner, C., & McNamara, D. P. (1984). Aircraft measurements of convective draft cores in MONEX. *Journal of the Atmospheric Sciences*, *41*(3), 430–438. https://doi.org/10.1175/1520-0469(1984)041<0430:AMOCDC>2.0.CO;2

Yang, B., Qian, Y., Lin, G., Leung, L. R., Rasch, P. J., Zhang, G. J., et al. (2013). Uncertainty quantification and parameter tuning in the CAM5 Zhang-Mcfarlane convection scheme and impact of improved convection on the global circulation and climate. *Journal of Geophysical Research: Atmospheres*, *118*(2), 395–415. https://doi.org/10.1029/2012JD018213

Yang, G.-Y., & Slingo, J. (2001). The diurnal cycle in the tropics. *Monthly Weather Review*, *129*(4), 784–801. https://doi.org/10.1175/1520-0493(2001)129<0784:TDCITT>2.0.CO;2

Yun, Y., Liu, C., Luo, Y., Liang, X., Huang, L., Chen, F., & Rasmmusen, R. (2020). Correction to: Convection-permitting regional climate simulation of warm-season precipitation over Eastern China. *Climate Dynamics*, *54*(5–6), 3227. https://doi.org/10.1007/s00382-020-05172-y

Zhang, Z., Varble, A., & Feng, Z. (2024a). Datasets for the publication "simulated convective cell and system growth bias dependencies on atmospheric instability and model resolution" [Dataset]. *Zenodo*. https://doi.org/10.5281/zenodo.10655168

Zhang, Z., Varble, A., & Feng, Z. (2024b). Software configuration for manuscript: Simulated convective cell and system growth bias dependencies on atmospheric instability and model resolution (v1.0). *Zenodo*. https://doi.org/10.5281/zenodo.13760822

Zhang, Z., Varble, A., Feng, Z., Hardin, J., & Zipser, E. (2021). Growth of mesoscale convective systems in observations and a seasonal convection-permitting simulation over Argentina. *Monthly Weather Review*, *149*(10), 3469–3490. https://doi.org/10.1175/mwr-d-20-0411.1